



HAL
open science

Intracerebral Injection of Graphene Oxide Nanosheets Mitigates Microglial Activation Without Inducing Acute Neurotoxicity: A Pilot Comparison to Other Nanomaterials

Corinne Portioli, Cyrill Bussy, Mariarosa Mazza, Neus Lozano, Dhifaf A. Jasim, Maurizio Prato, Alberto Bianco, Marina Bentivoglio, Kostas Kostarelos

► To cite this version:

Corinne Portioli, Cyrill Bussy, Mariarosa Mazza, Neus Lozano, Dhifaf A. Jasim, et al.. Intracerebral Injection of Graphene Oxide Nanosheets Mitigates Microglial Activation Without Inducing Acute Neurotoxicity: A Pilot Comparison to Other Nanomaterials. *Small*, 2020, 16 (48), pp.2004029. 10.1002/sml.202004029 . hal-04697592

HAL Id: hal-04697592

<https://hal.science/hal-04697592v1>

Submitted on 13 Sep 2024

HAL is a multi-disciplinary open access archive for the deposit and dissemination of scientific research documents, whether they are published or not. The documents may come from teaching and research institutions in France or abroad, or from public or private research centers.

L'archive ouverte pluridisciplinaire **HAL**, est destinée au dépôt et à la diffusion de documents scientifiques de niveau recherche, publiés ou non, émanant des établissements d'enseignement et de recherche français ou étrangers, des laboratoires publics ou privés.

Injection of Graphene Oxide Nanosheets in the Brain Does not Induce Acute Neurotoxicity and Counteracts the Acute Microglial Activation related to Surgery in a Pilot Study

Corinne Portioli^{1, 2, §}, Cyrill Bussy^{1, 3, 4 *}, Mariarosa Mazza¹, Neus Lozano^{1, 3}, Dhifaf A. Jasim^{1, 3}, Maurizio Prato^{5, 6}, Alberto Bianco⁷, Marina Bentivoglio² and Kostas Kostarelos^{1, 3, 8, *, &}

¹ *Nanomedicine Lab, School of Health Sciences, Faculty of Biology, Medicine & Health, The University of Manchester, Manchester Academic Health Science Centre, Manchester, UK*

² *Department of Neurosciences, Biomedicine and Movement Sciences, University of Verona, Verona, Italy*

³ *National Graphene Institute, The University of Manchester, Manchester, UK*

⁴ *Lydia Becker Institute of Immunology and Inflammation, Faculty of Biology, Medicine and Health, The University of Manchester, Manchester Academic Health Science Centre, Manchester, UK*

⁵ *Department of Chemical and Pharmaceutical Sciences, University of Trieste, 34127 Trieste, Italy*

⁶ *Carbon Nanobiotechnology Laboratory, CIC BiomaGUNE, 20009 San Sebastian, Spain.*

⁷ *University of Strasbourg, CNRS, Immunology, Immunopathology and Therapeutic Chemistry, UPR 3572, Strasbourg, France*

⁸ *Catalan Institute of Nanoscience and Nanotechnology (ICN2), and The Barcelona Institute of Science and Technology (BIST), Campus UAB, Bellaterra, Barcelona, Spain*

[§] Current address: Neuroscience and Brain Technologies Department, Istituto Italiano di Tecnologia (IIT), Genova, Italy and Verna and Marrs McLean Department of Biochemistry and Molecular Biology, Baylor College of Medicine (BCM), Houston, TX, United States

ORCID numbers:

Cyrill Bussy: 0000-0001-8870-443X

Dhifaf A. Jasim: 0000-0002-6433-4478

Alberto Bianco: 0000-0002-1090-296X

Marina Bentivoglio: 0000-0003-4958-9795

Kostas Kostarelos: 0000-0002-2224-6672

* To whom correspondence should be addressed:

kostas.kostarelos@manchester.ac.uk ; cyrill.bussy@manchester.ac.uk

& Lead contact: kostas.kostarelos@manchester.ac.uk

38 **Abstract**

39 Carbon-based nanomaterials (CNMs) are being explored for neurological applications. However,
40 systematic *in vivo* studies investigating the effects of CNM nanocarriers in the brain and how brain
41 cells respond to such nanomaterials are scarce. To address this, functionalised multi-walled carbon
42 nanotubes and graphene oxide (GO) sheets were injected in mice brain and compared with charged
43 liposomes. The induction of acute neuro-inflammatory and neurotoxic effects locally and in brain
44 structures distant from the injection site were assessed up to one week post-administration. While
45 significant neuronal cell loss and sustained microglial cell activation were observed after injection of
46 cationic liposomes, none of the tested CNMs induced either neurodegeneration or microglial
47 activation. Among the candidate nanocarriers tested, GO sheets appeared to elicit the least
48 deleterious neuro-inflammatory profile. At molecular level, GO induced moderate activation of pro-
49 inflammatory markers compared to vehicle control. At histological level, brain response to GO was
50 lower than after vehicle control injection, suggesting some capacity for GO to reduce the impact of
51 stereotactic injection on brain. While these findings are encouraging and valuable in the selection
52 and design of nanomaterial-based brain delivery systems, they warrant further investigations to
53 better understand the mechanisms underlying GO immunomodulatory properties in brain.

54

55

56

57 **Keywords**

58 Graphene – carbon nanotubes – liposomes – inflammation – brain – immunomodulation -
59 biocompatibility

60

61 Introduction

62 Nanomaterials may offer new solutions for unmet medical needs in the treatment of neurological
63 disorders [1-4]. Among the different types of nanomaterials suitable for these biomedical
64 applications, carbon-based nanomaterials (CNMs), including single-walled (SWNTs) or multi-walled
65 carbon nanotubes (MWNTs) and graphene have recently emerged as potential new candidates given
66 their remarkable interaction with the neural tissue [5-10]. CNMs possess unique physicochemical
67 properties, such as high surface area, mechanical strength, electrical conductivity [11-15] and the
68 ability to be chemically functionalised [16, 17]. In the context of neuroscience, these properties have
69 been shown to support neuronal activity [17] and facilitate drug delivery in the brain [18, 19].

70
71 Studies performed *in vitro* have for instance revealed the promising applications of functionalised
72 SWNTs as glutamate uptake enhancers in primary astrocytes [20] or as neuroprotective factors in
73 primary glial cells extracted from brains of an Alzheimer's disease (AD) mouse model [21]. Similarly,
74 in animal models, functionalised CNMs were efficient in delivering siRNA in a stroke model [22] or as
75 drug carrier in an AD model [23]. Another step toward their clinical translation was achieved when
76 the translocation of functionalised MWNTs (*f*-MWNTs) across the blood-brain barrier (BBB) was
77 demonstrated, initially *in vitro* [24, 25] and then *in vivo* [26, 27]. These seminal studies have paved
78 the way toward the targeted delivery of active therapeutics across the BBB after peripheral
79 administration of CNMs, as proposed in one proof-of-concept *in vivo* study for brain glioma [19]. More
80 recently, graphene-based materials (GBMs) and in particular Graphene Oxide (GO), the oxidised
81 form of graphene that results from chemical exfoliation of graphite, have also been explored for brain
82 therapy [6, 15]. Noticeably, GBMs were shown to inhibit the formation of β -amyloid aggregates and
83 could thus be beneficial in preventing the progression of AD [28]. Then, chemically functionalised GO
84 sheets were reported to be suitable photothermal platforms for destroying formed amyloid
85 aggregates in AD model upon near-infrared light irradiation, via the generation of localised heat [29,
86 30]. Finally, GBMs were used as nanocarriers for anti-tumour drugs in both *in vitro* and *in vivo*
87 models of brain cancer [18, 31], and as neurotransmission modulator with potential applications in
88 neurobiology [32].

89
90 However, a key issue for a more widespread use of nanocarriers (including CNMs) in brain therapy is
91 the response of the brain parenchyma once nanomaterials interact with the different cell populations
92 of the central nervous system (CNS). This becomes especially crucial in view of potential
93 applications of nanocarriers in brain diseases with an inherent neuro-inflammatory component, such
94 as neurodegeneration, stroke, infection or cancer [33-35]. Therefore, to support the exploration of the
95 full potential of CNMs for brain therapy applications, increasing effort has been devoted to investigate
96 the possible side effects of these materials upon interaction with the brain parenchyma. MWNTs
97 coated with polymeric material (Pluronic F127, used to increase solubility of MWNTs) were initially
98 incubated with primary cortical neurons [36]. As these MWNTs did not induce apoptotic effects *in*
99 *vitro*, their biocompatibility was then validated *in vivo* upon injection in the visual cortex of mice [36].
100 Similarly, no major tissue damages were reported in another study performed to analyse the neuro-

101 inflammation and cellular uptake of two types of *f*-MWNTs (carboxylated or amino-functionalised),
102 after injection in the cerebral cortex [37]. Both *f*-MWNT types were internalised by microglial cells and
103 neurons, and elicited a higher glial cell marker expression at the injection site, 2 days after injection
104 [37]. However, at 30 days post-injection, only carboxylated MWNTs resulted in persistent glial cell
105 activation in regions peripheral to the injection site [37]. In another set of studies, after the infusion of
106 PEGylated SWNTs in the hippocampus of rats, an antioxidant response was observed after 24 h [38]
107 and up to 7 days [39]. The authors theorised that the antioxidant response to SWCNTs could partly
108 explain the moderate impact of the nanomaterials on animal behaviours [38]; moreover, the
109 biopersistence of these CNMs at the injection site was ascribed for the persistence of the antioxidant
110 response over 7 days [39]. Lastly, a study on the neurotoxic effect of different *f*-MWNTs using
111 primary cultures of neuronal and glial cells derived from either the striatum or frontal cortex revealed
112 that while *f*-MWNTs did not affect neuronal cells from any of the two brain regions or glial cells from
113 the frontal cortex, the viability of striatum-derived glial cells decreased [40]. Although the brain
114 region-dependent cytotoxicity to glial cells was shown to be independent of the *f*-MWNT type, it was
115 instead associated with the number of microglial cells in the considered brain region-derived cell
116 cultures [40], highlighting the key role of microglial cells (the resident macrophages of the brain) in
117 the regulation of the biological response to CNMs.

118

119 More recently, the potential impact of GBMs on brain cells and tissue has also been explored.
120 Functionalised graphene-based systems investigated as drug delivery carriers in the treatment of
121 subarachnoid haemorrhage did not show neurotoxicity in the targeted region [41]. However, GO
122 sheets were reported to down-regulate neuronal activity and signalling *in vitro*, albeit without affecting
123 viability [42, 43]. Autophagy and calcium homeostasis were also found to be disturbed in neuron
124 cultures exposed to GO, highlighting the ability of GO sheets to damage neuronal transmission and
125 functionality, without inducing toxicity [43]. Astrocyte function and homeostasis were similarly altered
126 by GO sheet exposure and internalisation, subsequently impacting the neuronal network that
127 astrocytes were supporting [44]. Finally, when primary mixed glia or the microglia BV2 cell line were
128 pre-treated with GO sheets, inhibition of NLRP3 inflammasome-dependent interleukin (IL)-1 β
129 secretion was observed upon lipopolysaccharide (LPS) and ATP priming [45].

130

131 Despite this growing knowledge and the great potential of CNMs as brain drug delivery vectors,
132 systematic studies assessing the inflammatory potential of these nanocarriers in brain tissue remain
133 scarce. To address this gap, three different types of engineered CNMs, including one GO type and
134 two *f*-MWNTs (aminated or carboxylated), were here injected stereotactically into the striatum of mice
135 and their potent inflammation was assessed. For comparison, two types of highly charged liposomes
136 were used as benchmark drug delivery systems with previously reported tissue [46, 47] and brain
137 [48, 49] inflammogenicity. Considering recent findings highlighting the immunomodulatory and anti-
138 inflammatory properties of GO sheets *in vitro* and *in vivo* [32, 45, 50], the present study was also
139 designed to test the hypothesis that GO materials present a unique inflammation profile when
140 compared to other nanomaterials. The inflammatory potential of the different candidate nanocarriers

141 was therefore assessed at different time points of the acute early stage response (up to 1 week after
142 injection) at both the molecular (i.e. transcripts encoding a panel of cytokines and chemokines) and
143 histological (i.e. activation of astrocytes and microglial cells, number of neurons and dead cells)
144 levels. These analyses were performed not only at the injection site (central position in the striatum)
145 but also in adjacent and distant positions within the brain, to assess both the diffusion of inflammation
146 processes and the delocalised effects caused by nanomaterial diffusion.

147

148 **Results**

149 **Characterisation of the NMs**

150 Either aminated or carboxylated *f*-MWNTs that have been previously explored for biomedical
151 applications were used in the present study [22, 37, 51-54]. Their chemical functionalization is
152 thought to not only improve solubility, but also increase biocompatibility by reducing toxicity through
153 mitigation of the material-cell membrane interaction. The dimensional features (diameter and length)
154 of those *f*-MWNTs were analysed by transmission electron microscopy (TEM; **Figure 1-B**, and **S1-**
155 **A**). Both types of *f*-MWNTs had an outer diameter between 20 and 30 nm. Carboxylated *f*-MWCNTs
156 (ox-MWNTs) were between 200 and 300 nm in length, while aminated *f*-MWNTs (MWNT-NH₃⁺) had
157 a length between 500 nm and 2000 nm. The Kaiser test was performed to establish the amount of
158 amino groups present on the MWNT-NH₃⁺, and found a loading of 58 μmol/g of amino functional
159 groups (**Figure S1-A**); while the amount of carboxyl group on the ox-MWNTs had been previously
160 determined using thermogravimetric analysis and found a loading of 1,7 μmol/g [55].

161

162 In line with our previous works, several techniques were used to assess the physicochemical
163 properties of GO sheets (**Figures 1-B** and **S1-B**). The ζ-potential was -50.0 ± 0.4 mV. The lateral
164 dimensions were established with TEM and were in between 10 and 1800 nm, while atomic force
165 microscopy (AFM) revealed a thickness between 0.9 and 4.8 nm, consistent with few layer 2D
166 materials, as we previously reported [56, 57].

167

168 Characterisation of cationic (DOTAP:Chol) and anionic (DOPG:Chol) liposomes was performed to
169 confirm their hydrodynamic diameter size, polydispersity index (PDI) and ζ-potential (**Figures 1-B**
170 **and S1-C**). Cationic (DOTAP:Chol) and anionic (DOPG:Chol) liposomes showed a hydrodynamic
171 diameter of 125.6 ± 2.6 nm and 118.1 ± 3.0 nm, respectively. DOTAP:Chol liposomes showed a PDI
172 of 0.254 ± 0.004 , while in the case of DOPG:Chol liposomes, the PDI was 0.393 ± 0.061 . The
173 surface charge of the liposomes was confirmed by ζ-potential measurements. DOTAP:Chol
174 liposomes were formed by positively charged polar chains (DOTAP, **Figure S1-C**) that attribute the
175 cationic nature to the system ($\zeta = +60.5 \pm 2.6$ mV), while DOPG:Chol liposomes were formed by
176 negatively charged polar chains (DOPG, **Figure S1-C**) that attribute the anionic nature to the system
177 ($\zeta = -54.1 \pm 0.5$ mV).

178

179

180 **Expression of inflammation-related genes**

181 The gene expression levels of transcripts encoding inflammatory molecules were measured in the
182 sampled brain tissue blocks. Transcripts encoding TNF- α , IL-1 β , IFN- γ , IL-6 and IL-12 were used to
183 evaluate pro-inflammatory cytokines, CCL2 and CXCL10 as pro-inflammatory chemokines, and IL-
184 10, IL-4 and TGF- β as anti-inflammatory markers (**Table S1**).

185

186 **Central brain injection site**

187 The gene expression results for inflammatory markers in the injection site (central striatum) are
188 presented in **Figure 2**. As expected, bacterial LPS injection (positive inflammation control) induced
189 significantly higher expression levels for all inflammatory transcripts tested, except for *ifn- γ* mRNA at
190 day 1 and *cxcl10* mRNA at day 1 and 2. At day 7, the upregulation of inflammatory transcripts
191 induced by LPS was lower than at the two shorter time points, but remained significantly different
192 from *il-10* mRNA induced by dextrose injection. Surprisingly, there was no significant upregulation of
193 *cxcl10* expression at any time point.

194

195 In contrast, carbon nanomaterials had a limited effect on the expression levels of these genes
196 (**Figure 2**). Over time, ox-MWNTs had a limited impact at day 1 (upregulation of *tnf- α* and *il-1 β*
197 mRNAs), high impact at day 2 (upregulation of *il-12*, *ifn- γ* , *il-6* and *tgf- β* mRNAs) and returned to
198 basal levels at day 7. Similarly, GO upregulated only *tgf- β* expression at day 1, upregulated *tnf- α* and
199 *il-6* expression at day 2, but had no effect at day 7. MWNT-NH₃⁺ upregulated only the *il-6* gene at
200 both day 1 and 2 but had no effect at day 7. Comparison of the three carbon NMs revealed that
201 MWNT-NH₃⁺ had the safest inflammatory profile at day 1 while GO was the safest at day 7. At day 2,
202 both MWNT-NH₃⁺ and GO behaved similarly, while ox-MWNTs induced the greatest inflammation.

203

204 Liposomes were used here as positive nanomaterial controls and were found to more broadly affect
205 gene expression (**Figure 2**). DOTAP:Chol upregulated *il-6* and *il-10* mRNAs at day 1; this
206 upregulation persisted at day 2, when expression levels of *tnf- α* , *il-1 β* and *tgf- β* mRNAs were also
207 upregulated. In addition, the inflammation induced by DOTAP:Chol was maintained at day 7 with
208 upregulation of *ifn- γ* , *ccl2* and *cxcl10* gene transcripts. Similarly, DOPG:Chol upregulated *il-12*, *il-6*
209 and *il-10* mRNAs at day 1 and upregulated *tnf- α* , *il-1 β* , *il-12*, *il-10* and *ccl2* expression at day 2 but
210 returned to basal level at day 7. When comparing the two types of liposomes, no significant
211 differences were observed for any inflammatory marker at day 1. At day 2, significant differences
212 were found for *ccl2* mRNA only. At day 7, significant differences were found for *tnf- α* , *ifn- γ* , *il-12*, *ccl2*
213 and *cxcl10* mRNAs, revealing an accentuated pro-inflammatory profile for cationic DOTAP:Chol
214 liposomes in comparison to anionic DOPG:Chol liposomes.

215

216 Among the different NMs, carbon NMs appeared to elicit the mildest inflammatory response at the
217 injection site. Both MWNT-NH₃⁺ and GO yielded similar results, whereas ox-MWNT was the most
218 pro-inflammatory NM, especially at day 1 and 2 post-injection.

219

220 **Adjacent posterior brain region**

221 The results of gene expression for different inflammatory markers in the posterior brain region in
222 direct contact with the injection site are presented in **Figure S2**. After LPS injection, upregulation of
223 transcript levels for all markers followed the same trends as in the site of injection. At day 1 and 2, all
224 transcripts were upregulated except for *ifn- γ* mRNA at day 1. At day 7, expression of the *tnf- α* and *il-
225 1 β* genes were still upregulated.

226

227 At day 1, carbon NMs had no significant impact on the expression of any of the genes tested in this
228 brain region (**Figure S2**). At day 2, all three carbon NMs regardless of their characteristics
229 significantly downregulated *tnf- α* expression and upregulated *ccl2* expression. At day 7, none of the
230 carbon NMs had any significant effect. No significant differences were observed at any time point
231 among the three carbon NMs, despite a trend suggesting a mild (compared to nanotubes)
232 inflammatory profile after GO administration, especially at day 7 (*i.e.* *ccl2*, *il-12*, and *ifn- γ* mRNAs had
233 lower values, albeit without statistical significance).

234

235 In contrast, following injection of liposomes, DOPG:Chol significantly upregulated *ccl2* and *cxcl10*
236 mRNAs at day 1, whereas DOTAP:Chol had no effect in the posterior brain region (**Figure S2**). At
237 day 2, while DOTAP:Chol significantly upregulated *il-1 β* and *il-10* transcripts, DOPG:Chol
238 upregulated *tnf- α* and *ccl2* mRNAs. At day 7, none of the liposomes had any effect on inflammatory
239 marker gene expression, highlighting the transient inflammatory impact of these materials, possibly
240 due to their well-known poor long-term structural stability in living tissue.

241

242 **Distant anterior brain region**

243 Gene expression levels for the inflammatory markers in the anterior brain region (distant from the
244 injection site) are presented in **Figure S3**. As described above, at day 7 in the posterior brain region
245 (in direct contact with the injection site), a drastic decrease of the inflammatory response for all
246 markers and conditions tested was observed, including LPS injection (**Figure S2**). We therefore
247 reasoned that in a distant brain site (not in direct contact with the site of injection) inflammation levels
248 at day 7 would be even lower. This led us to investigate gene transcripts in the distant anterior brain
249 region only at day 1 and 2 (**Figure S3**). A second motivation for performing analyses of gene
250 transcripts in the anterior striatum after injection in the middle/central striatum (these two parts of the
251 striatum being at relative distance from each other) was brought about the hypothesis that liposomes
252 can diffuse across this brain region and therefore induce inflammation beyond the site of injection
253 [58, 59]. In addition, analyses were performed only for liposomes, as they were inducing upregulation
254 of genes in the posterior brain region (**Figure S2**), whereas all carbon NMs did not induce any gene
255 upregulation in this brain region (**Figure S2**).

256

257 The results following LPS injection in the anterior brain region were identical to those found for the
258 posterior brain region at day 1 and 2, with an upregulation of all markers except for *ifn- γ* expression
259 at day 1 (**Figure S3**). At day 1, anionic DOPG:Chol liposomes elicited the greatest inflammatory

260 response, with significant upregulation of *tnf- α* , *il-1 β* , *il-6*, *ccl2* and *cxcl10* mRNAs, whereas cationic
261 DOTAP:Chol only upregulated *il-1 β* expression. In contrast, DOTAP:Chol liposomes were more
262 inflammatory at day 2, with upregulation of *tnf- α* , *il-1 β* , *ccl2* and *cxcl10* expression, while DOPG:Chol
263 liposomes only upregulated *il-12* expression.

264

265 Overall, anionic DOPG:Chol liposomes seemed to have a greater inflammatory potential at day 1 and
266 2 not only at the injection site but also in nearby and distant regions of the brain. In contrast, cationic
267 DOTAP:Chol liposomes showed a greater inflammatory potential at day 2 in all brain regions,
268 persisting at day 7 only in the site of injection. These results suggested that liposomes, as
269 hypothesised, can diffuse across the brain tissue from the injection site and mediate pro-
270 inflammatory effects along their path.

271

272 **Impact on microglial cells and astrocytes**

273 To investigate the effect of the tested NMs on microglial cells and astrocytes, we focused our efforts
274 on day 2. This time point was selected based on the molecular findings presented above, which
275 indicates that expression levels of pro-inflammatory transcripts were higher 2 days after injection
276 than at the other time points. The same three brain regions assessed for the RT-qPCR analyses
277 were used for the histology study (**Figure 1-A**).

278

279 Glial cell analyses were based on CD11b and GFAP immunophenotyping. Both qualitative
280 observations of cell features to detect structural changes indicating an activated state (such as cell
281 body hypertrophy and increased thickness of processes) and quantitative analyses were performed
282 (CD11b, **Figure 3 -Ai, -Bi, and -Ci**; GFAP, **Figure 3 -Aii, -Bii, and -Cii**). The latter evaluated the
283 following different parameters: *i*) area covered by microglia and astrocytes, including cell branches (a
284 higher area indicating cell hypertrophy) (**Figures S4-A and S5-A**), *ii*) intensity of microglial cell
285 immunoreactivity evaluated by densitometry (increased intensity indicating CD11b upregulation)
286 (**Figure S4-B**) and *iii*) astrocyte cell number (an increased cell number indicates astrocytic activation)
287 (**Figure S5-B**).

288 The area covered by microglial cells (**Figure 3 -Ai, -Bi, and -Ci**) and astrocytes (**Figure 3 -Aii, -Bii,**
289 **and -Cii**) was evaluated for all conditions tested and in the three brain regions considered. The
290 analysis was also conducted in matched regions of the contralateral hemisphere to obtain data in
291 tissue devoid of mechanical trauma due to stereotactic injection or surgery.

292

293 **Microglial cells**

294 Immunolabelled microglial cells at the injection site did not show features of activation, or only mild
295 activation in comparison to vehicle control (5% dextrose in water), at day 2 after injection (**Figures**
296 **S4-A and 3-Bi**). This was observed for all NMs and doses tested here. Only injection of cationic
297 DOTAP:Chol or anionic DOPG:Chol liposomes replicated the features observed after LPS injection
298 (*i.e.* hypertrophy and “bushy” appearance of microglial cells). However, this was not significantly
299 different from the vehicle control, as analysed quantitatively (**Figure 3-Bi**). High cell death, likely

300 involving both neurons and glia, was observed at the site of injection after either of these liposomal
301 treatments and could account for this finding. Surprisingly, GO injections at 1 mg/ml resulted in
302 significantly lower CD11b immunoreactivity than control vehicle injection and was similar to that
303 observed in the contralateral non-injected hemisphere (**Figure 3-Bi**). Administration of either type of
304 *f*-MWNTs at both 0.5 and 1 mg/ml and GO at 0.5 mg/ml induced a glial cell activation comparable to
305 that observed after vehicle injection.

306

307 In brain tissue sections distant from the injection site (i.e. anterior brain region), weak microglial cell
308 activation was observed after NM injections, while LPS induced clear microglial cell activation
309 (**Figure S4-A**). When analysed quantitatively and in comparison to the contralateral region, only LPS
310 injection elicited a significant activation of CD11b-positive cells (**Figure 3-Ai**). All the other conditions,
311 including both types of *f*-MWNTs or liposomes and GO, induced microglial cell activation at a level
312 similar to that induced by vehicle injection or even lower, and was similar to that observed in the
313 contralateral hemisphere. Only cationic DOTAP:Chol liposomes (and to a lesser extent DOPG:Chol
314 liposomes) induced microglial cell activation that was slightly more pronounced (but not significant)
315 than the vehicle.

316

317 In sections from brain tissue in direct contact with the injection site (i.e. posterior brain region), mild
318 activation of microglial cells was observed after injection of LPS and anionic DOPG:Chol liposomes;
319 this was also observed to a lesser extent after cationic DOTAP:Chol liposome injection (**Figure S4-**
320 **A**). Accordingly, quantitative evaluation of the percentage of the area covered by CD11b-positive
321 cells showed a significant increase only in brains after LPS or DOPG:Chol liposome injection (**Figure**
322 **3-Ci**). DOTAP:Chol injection induced a modest, but not significant, increase of CD11b-positive cell
323 coverage compared with both vehicle control injection and the contralateral region. Both types of *f*-
324 MWNTs at either concentration had no effect on activation of microglial cells in this region with
325 results similar to vehicle control injection. Noticeably, GO injection at either concentration resulted in
326 a lower signal than the vehicle and was more comparable to the contralateral region, albeit not
327 significantly.

328

329 Based on these results, particularly the surprising results obtained with GO *versus* liposomes or *f*-
330 MWNTs, a densitometric evaluation of CD11b immunostaining intensity was performed in brain
331 sections containing the injection site and compared against results obtained from LPS- and vehicle-
332 injected brain tissues (**Figure S4-B**). Consistent with the findings mentioned above, densitometric
333 analysis revealed a significantly lower CD11b optical density after administration of GO than after
334 vehicle, at the two tested GO doses. These results suggest that the presence of GO could be
335 beneficial in reducing the trauma of surgical injection in the striatum. In contrast, and as expected,
336 CD11b optical density after LPS injection was significantly higher than vehicle injection. Differences
337 in this parameter between injection of DOTAP:Chol or DOPG:Chol liposomes and vehicle were not
338 significant.

339

340 **Astrocytes**

341 Hypertrophic astrocytes, as indicated by higher GFAP immunoreactivity, were observed after LPS
342 injection at the injection site (**Figure S5-A**). Accordingly, the relative surface area covered by
343 astrocytes after LPS injection showed a significant increase when compared with vehicle control
344 injection (**Figure 3-Bii**). Although not significant, the area covered by GFAP-positive cells was also
345 slightly increased after injection of ox-MWNT at both concentrations or injection of anionic
346 DOPG:Chol liposomes when compared with vehicle. None of the other NMs induced significant
347 differences when compared with vehicle control injections, but all conditions induced higher astrocyte
348 coverage than in the matched, contralateral non-injected brain regions; this suggests that the
349 mechanical trauma due to their respective injections could account for this mild astrocytic reaction.

350

351 In brain sections from the anterior region (distant from site of injection), mild features of astrocyte
352 activation were observed after administration of LPS or cationic DOTAP:Chol liposomes (**Figure S5-**
353 **A**). Accordingly, the relative surface area of the brain tissue covered by GFAP immunoreactivity was
354 significantly higher after injection of LPS and DOTAP:Chol liposomes than after vehicle, although
355 values were lower after injection of DOTAP:Chol than LPS (**Figure 3-Aii**). None of the other NMs
356 induced significant differences. Although not significant, values were lower after GO injection than
357 after vehicle injection (for both GO doses tested) and were similar to the contralateral hemisphere,
358 consistent with the results for microglial cell reactivity after GO treatment. For all conditions, the
359 relative surface area of the tissue covered by GFAP immunoreactivity was overall lower in this
360 anterior brain region than at the injection site (**Figure 3-Aii and -Bii**).

361

362 In the posterior brain region (*i.e.* sections in close vicinity to the injection site), astrocyte activation
363 was observed only after LPS injection and to a far lesser extent after DOTAP:Chol or DOPG:Chol
364 liposome injection (**Figure S5-A**). Astrocytes had normal appearance for every other condition.
365 These observations were supported by quantitative evaluation of the area covered by GFAP
366 immunoreactivity (**Figure 3-Cii**). Only LPS induced a significant increase of GFAP coverage. Values
367 after DOTAP:Chol or DOPG:Chol liposome injection were slightly higher than after vehicle
368 administration, while every other condition showed values similar to or lower than vehicle-injected
369 controls. Noticeably, values after GO at 1 mg/ml were lower than after vehicle injection and similar to
370 those in the matched contralateral brain region.

371

372 Considering these results and the higher astrocyte activation observed in the anterior brain region
373 after injection of cationic DOTAP:Chol liposomes, astrocyte cell number was analysed after injection
374 of DOTAP:Chol liposomes and compared to both positive (LPS) and negative (vehicle) controls
375 (**Figure S5-B**). DOTAP:Chol liposome injection did not significantly affect the number of astrocytes in
376 the three analysed brain regions, despite being higher than the vehicle control in the anterior brain
377 region. The latter result was concordant with the relative coverage of GFAP-positive cells in
378 DOTAP:Chol liposome-injected brains (**Figure 3**), which showed greater astrocyte activation than
379 after vehicle injection but lower than after LPS injection. Astrocyte number was also significantly

380 increased in the anterior and posterior brain regions after LPS injection, but was not significantly
381 increased in the injection site. These findings were also in agreement with the relative coverage of
382 GFAP-positive cells that showed that LPS resulted in higher values in both the anterior and posterior
383 brain regions (**Figure 3-Aii** and **-Cii**) than in the injection site (**Figure 3-E**) when compared with
384 vehicle. As mentioned above, this could be explained by the high cell death (involving glia) elicited by
385 LPS in the injection site (**Figure 3-Bii**).

386

387 **Impact on neuronal cell viability**

388 Akin to glial cells, the impact of the different NMs on neurons was also studied at day 2 after
389 injection. Neuronal cell death following injection of NMs was quantified using NeuN immunostaining
390 (**Figure S6**). Statistical evaluation was performed by comparing each data set with that obtained after
391 vehicle injection in the respective brain region (**Figure 3 -Aiii**, **-Biii**, and **-Ciii**). Only in the injection
392 site and after LPS or cationic DOTAP:Chol liposome injections was a significant loss of neurons
393 observed (**Figure 3-Biii**). LPS induced higher neuronal cell loss compared to DOTAP:Chol. No
394 significant neuronal cell loss was observed after injection of the other NMs or in the other two brain
395 regions.

396

397 Based on neuronal cell loss, the number of apoptotic cells were analysed measuring the cleaved
398 caspase 3 immunoreactivity after LPS and cationic DOTAP:Chol liposome injections, and were
399 compared to vehicle and GO injections (**Figure 4**). The greatest number of cleaved caspase 3
400 positive cells was found in brain sections containing the injection site after LPS or cationic liposome
401 injections, in agreement with the loss of NeuN immunoreactivity. Interestingly, a greater number of
402 cleaved caspase 3 positive cells was also observed in the cerebral cortex at the level of the injection
403 site, possibly associated with the needle track passing through the cortex to reach the striatum, but
404 only after LPS and DOTAP:Chol liposome injections and not after vehicle or GO injections. This
405 suggests a safer toxicological profile for GO than DOTAP:Chol liposomes, consistent with the results
406 obtained with CD11b immunoreactivity (**Figure S3-B**).

407

408 Finally, a Fluoro-Jade B staining was performed (**Figure S7**) to label neurons undergoing
409 degeneration [60]. Combining Fluoro-Jade B staining with cleaved caspase 3 staining would help
410 confirming whether cleaved caspase 3 positive cells were in fact neurons. Consistent with both the
411 NeuN and cleaved caspase 3 signals, only LPS-injected brains had Fluoro-Jade B labelled neurons
412 in the striatum. In the cortical tissue surrounding the needle track, a limited number of Fluoro-Jade B
413 positive cells were observed after injection of LPS, DOTAP:Chol liposomes, or (to a lesser extent)
414 vehicle. Surprisingly, no Fluoro-Jade B stained cells were observed after GO injection in the striatal
415 or cortical regions, suggesting that the presence of GO sheets may have prevented the brain tissue
416 damages associated to surgery and observed after vehicle injection, which supports the data
417 obtained with CD11b immunoreactivity (**Figure S4-B**). Results from NeuN and cleaved caspase 3
418 immunostaining clearly revealed that NMs inducing neurotoxicity (*i.e.* DOTAP:Chol liposomes) were
419 only detrimental at the site of injection, but not in adjacent brain regions. This finding was suggesting

420 that, despite the potency of these materials to diffuse across the brain tissue (as indicated by their
421 inflammatory potential across the three tested regions), the amount of diffusing materials is likely to
422 be limited, or that neurotoxicity requires a high dose of materials, such as found at the injection site,
423 to occur.

424

425 Taken together, the results obtained with NeuN, cleaved caspase 3 and Fluoro-Jade B indicate that
426 only cationic DOTAP:Chol liposomes (and the positive control for inflammation, LPS) had a clear
427 negative impact on cells and primarily at the site of injection. In contrast, GO appears to have a safer
428 and potentially beneficial profile in respect to neurons.

429

430 **Discussion**

431 Due to their unique properties and dimensions, engineered nanomaterials have emerged as novel
432 nanomedicine solutions for the treatment or diagnosis of various neurological conditions [1].

433 However, the CNS is a very sensitive environment. If freely bioavailable in the brain parenchyma,
434 nano-sized foreign materials such as nanocarriers may easily cause disruption to physiological
435 processes and functions. It is therefore of greatest importance that safety considerations are
436 implemented at an early stage during the development of biomedical nanomaterials for CNS
437 applications [61]. For this to happen, a better understanding of the nanomaterial physicochemical
438 characteristics that may induce adverse effects in the brain, such as inflammation, is warranted. This
439 is particularly essential for biomedical nanomaterials developed to treat brain diseases that already
440 have an inflammatory component [34, 35].

441

442 Recently, both carbon nanotubes and graphene-based materials have shown great promise for the
443 treatment and imaging of neurological disorders. However, there is a limited number of studies that
444 have specifically explored the neuro-inflammation profiles of these CNMs in the brain. With this in
445 mind, we went on investigating the neuro-inflammatory potential of different CNMs that could
446 potentially be used as brain nanomedicines. The tested nanocarriers were directly injected in the
447 striatum, which was used here as a model of centrally positioned brain region for assessing the
448 reactions of the three main cell types of the brain (namely neurons, astrocytes, and microglial cells)
449 to exogenous materials. Along with CNMs, both cationic and anionic liposomes were used as
450 benchmark materials with known inflammatory properties in various tissues [46, 47] or the brain [48,
451 49, 62]. These inflammatory properties are due to their high density of surface charges. Indeed, while
452 anionic micelles were shown to be well tolerated regardless of administration modalities [48], cationic
453 micelles and cationic liposomes elicited immune cell infiltration and neuronal degeneration due to
454 inflammatory response after central administration [48, 49].

455

456 In the present study, the inflammatory potential of the different nanomaterials was then tested at both
457 molecular and histological levels. These investigations were performed not only in the area of the brain
458 injected with the candidate nanocarriers, but also in adjacent brain areas, either in close vicinity to the

459 site of injection (*posterior area*) or a few mm away from the site of injection (*anterior area*). This
460 assessment in three different locations of the same striatum was designed to assess the possible
461 diffusion of the materials or biological effects (or both) across the injected brain region, namely the
462 striatum. In addition, different doses of nanomaterials were considered. The main tested dose for *f*-
463 MWNTs and GO (*i.e.* 0.5 µg) was based on previous studies for drug delivery purposes using similar
464 administration route, bypassing the blood brain barrier [22, 53]. This amount was then doubled to
465 directly compare with the dose used for liposomes and to assess the role of positive and negative
466 charges in the inflammation profile of surface-charged CNMs, such as functionalised MWNTs and GO.
467 All tested materials were compared to a negative control, an injection with the vehicle (5% dextrose in
468 water), which reflected the background inflammatory response to the brain tissue damage induced by
469 the stereotactic surgical procedure. The reported neuro-inflammation profiles for the different
470 nanomaterials tested are therefore representing not only the brain tissue response to the material
471 injections, but also how each tested nanomaterial modulated the inflammatory response inherent to
472 the brain surgery used to administer those materials [50]. NM treatments were also compared to LPS,
473 a known inflammogenic compound.

474

475 Gene expression analyses of pro- and anti-inflammatory markers revealed that the tested
476 nanomaterials elicited different patterns of inflammatory response in the considered brain areas. In
477 general, regardless of their nature, the levels of pro-inflammatory markers after the administration of
478 nanomaterials were found to be significantly lower than those elicited by LPS injection at days 1 and
479 2, when the LPS-induced upregulation was greatest. But an overall mild acute neuro-inflammatory
480 response was found for all the different nanomaterials tested, in comparison to the negative control.
481 Although the administration of carbon NMs, including GO, elicited a mild upregulation of pro-
482 inflammatory transcripts immediately after injection, still observable at day 2, gene expression levels
483 for these materials were comparable to the negative control by day 7. These findings are in
484 agreement with previous investigations in which *f*-MWNTs that were either carboxylated and
485 aminated or aminated only, had been injected in the cerebral cortex of mice and induced in both
486 cases a transient inflammatory reaction, attributed to both nanomaterial and brain surgery, with brain
487 tissue showing no signs of inflammation by day 14 [37]. Contrastingly, injection of cationic liposomes
488 induced marked levels of transcripts encoding pro-inflammatory markers (particularly at the site of
489 injection) that persisted for up to 7-day after injection, in agreement with previous studies [48, 49].

490

491 In brain regions close to (but not within) the injection site, there was an overall lower level of pro-
492 inflammatory transcripts compared to the injection site. Apart from day 2, the administration of *f*-
493 MWNTs and GO did not elicit upregulation of any pro-inflammatory mediators in a nearby brain
494 region from the injection site, which is consistent with a previous study that did not reveal any
495 diffusion of the biological effects after intra-cerebroventricular injection [37]. However, despite the
496 distance from the injection site, the administration of cationic liposomes induced marked upregulation
497 of inflammatory markers in these brain regions at both day 1 and 2. This suggests potential diffusion
498 of either the biological response via intercellular signalling, possibly mediated by activated microglial

499 cells, or the nanomaterials (or both). This observation is consistent with observations by Knudsen *et*
500 *al.* [48]. In this study, macrophage infiltration was observed both in the injection site and in a nearby
501 brain region 1 week after the injection of cationic and anionic liposomes in the dentate gyrus of rats.

502

503 Neurotoxicity leading to neurodegenerative effects represents a major concern for the use of
504 nanocarriers in the brain [54]. The results obtained in the present study did not reveal acute neuronal
505 cell death effects for most of the analysed nanomaterials. Indeed, cell counting revealed a significant
506 decrease of neuronal cell number in the injection site only after administration of cationic liposomes.
507 These findings are consistent with results obtained in a previous study in which the potential
508 systemic and central toxic responses were evaluated after brain administration of non-PEGylated
509 cationic (DOTAP:Chol-Chol) liposomes or PEGylated micelles that were either cationic or anionic
510 [48]. In the latter study, intra-cerebroventricular administration of cationic liposomes induced
511 inflammatory cell infiltration, neuronal degeneration, and cell apoptosis, whereas the administration
512 of anionic particles did not cause any toxic reaction [48]. Similarly, in the present study, the
513 DOPG:Chol anionic liposomes did not induce neurotoxicity, while cationic DOTAP:Chol liposomes
514 resulted in neurotoxic effects. However, while LPS elicited glial and neuronal cell death at the site of
515 injection, cationic liposomes only affected neuron cell number. This could be due to the properties of
516 cationic liposomes, which are instable nanosystems characterised by rapid clearance due to fusion
517 with cell membranes, hence are short-lived [63].

518

519 In contrast to liposomes, regardless of their surface charge none of the CNMs induced neurotoxicity.
520 This is consistent with a previous long-term (12 w or 1 y) experimental study on brain tissue
521 response following the injection of nanowires with different lengths (2, 5, and 10 μm) in which no
522 significant differences in the number of neurons were measured [59]. In another study, PEGylated
523 SWNTs did not induce cerebral tissue damage or cognitive function alterations at 1 or 7 days after
524 infusion in the rat hippocampus [39]. In addition, despite short-term oxidative damage observed at 30
525 min, an unanticipated antioxidant effect was observed after 7 days, suggesting a potential
526 neuroprotective ability of these functionalised carbon nanotubes [39].

527

528 The brain inflammatory response to nanocarrier injection is expected to be mediated by glial cells,
529 since both microglia and astrocytes act as scavengers for maintaining homeostasis and signalling
530 between cells. On one hand, astrocytes control ion and nutrient balance [64], and are activated upon
531 injury, which manifests structurally by an hypertrophy of the cell body and processes, and an
532 upregulation of GFAP [65]. On the other hand, microglial cells are the main CNS immune-resident
533 components, reacting to early changes in neuronal activity or to pathological conditions [66] and
534 constitute the main defence mechanism in the brain. Therefore, the responses of both microglial cells
535 and astrocytes were analysed in detail in the present study.

536

537 At the injection site, no activation of microglial cells was observed after injection of CNMs, regardless
538 of their type or surface charge, whereas hypertrophic microglial cells were observed after injection of

539 liposomes (also regardless of their surface charge). Interestingly, in the brain region adjacent to
540 injection, mild microglia activation was observed after administration of both positively-charged amino
541 *f*-MWNTs and liposomes (anionic or cationic). These findings are consistent with a previous study in
542 which a local inflammatory response was induced by *f*-MWNTs [37]. In addition, a mild astrocyte
543 response was observed here at the injection site 2 days after injection, particularly after
544 administration of ox-MWNTs and anionic liposomes. In adjacent or distant brain regions, the
545 astrocyte response was significantly lower with respect to the injection site. A previous *in vitro* study,
546 performed on primary mixed glial cell cultures, emphasised the importance of microglial cells and
547 how their number (with respect to other cells such as astrocytes) can affect biological outcomes [40].
548 We observed that administration of cationic liposomes induced astrocyte activation at a distance from
549 the injection site, consistent with the pro-inflammatory gene expression response observed in the
550 same brain region with RT-qPCR analyses. These findings agree well with results obtained in a
551 previous study in which both astrogliosis and microgliosis (based on GFAP and Iba1
552 immunostaining) were identified directly at the site of injection of cationic micelles or in nearby brain
553 regions [48]. In contrast, anionic micelles did not induce a similar activation, highlighting the safer
554 profile of negatively charged nanomaterials when compared to positively charged nanomaterials.
555 Indeed, anionic particles interact less with cell membranes that are negatively charged surface. In
556 contrast, cationic particles, due to a higher electrostatic interaction with negatively charged cells, can
557 accumulate to a greater extent in cells and create a more significant burden. This in turn increases
558 the potential of positively charged nanomaterials to exert a toxic effect [67, 68].

559

560 Regarding the overall brain inflammation potential of the different nanomaterials tested here, GO
561 nanosheets appeared to have the least inflammatory profile, when combining both molecular and
562 histological results. This is consistent with a recent review that mentioned that, thus far, graphene-
563 based nanomaterials (including GO) appear to be safer than carbon nanotubes [69]. When
564 comparing carbon nanotubes and carbon based two-dimensional lattices, not only the dimensions
565 (lateral, thickness or length) but also physicochemical features such as rigidity/stiffness or
566 bioavailable surface area could be amongst the explanatory material factors making GO more
567 tolerable than MWNTs under the tested conditions [70, 71]. However systematic investigations
568 addressing those questions and comparing the two types of materials are lacking so far, in both the
569 nanotoxicology and nanomedicine literatures. Here, we observed that GO nanosheets not only
570 induced a moderate and acute inflammatory response (*tgf-β* over-expressed at day 1; *tnf-α* and *il-6*
571 over-expressed at day 2; expression levels similar to negative control for all transcripts by day 7), but
572 also led to a lower level of glial cell activation at day 2 when compared to vehicle injection (i.e. glial
573 activation due solely to surgery in this later case), especially at the 1 mg/mL dose. In addition, GO
574 induced less neurotoxicity than LPS, cationic liposomes, or even the vehicle control. This suggests
575 that the presence of GO in the brain could be beneficial to reduce the impact of intra-parenchymal
576 stereotactic surgical injection of materials, a traumatic injury that causes inflammation and cell death
577 by itself, as evidenced in the negative control results reported here. These findings are consistent
578 with a study [50] that reported that mouse brain directly injected with GO had lower GFAP

579 immunoreactivity at 48 h and lower iba1 immunoreactivity at 72 h after injection compared to
580 negative vehicle control, suggesting that GO had the capacity to lower the activation of astrocytes
581 and microglial cells, both caused by the brain surgery at the injection site. In agreement with this,
582 another study reported the immunomodulatory effects of GO pre-treatment on the macrophage
583 response to inflammatory challenge [45]. In this study, GO pre-treatment had an anti-inflammatory
584 effect upon activation of the inflammasome. Specifically, GO sheets reduced the release of IL-1 β and
585 IL-6 by an NRF2-mediated mechanism. This effect was observed not only in immortalised bone
586 marrow-derived macrophages but also in a primary murine mixed glia and immortalised microglia
587 BV2 cell line. While all these converging findings, including ours, are encouraging from a biomedical
588 perspective, they warrant further investigations to fully understand the underlying mechanism of the
589 immunomodulatory effects of GO nanosheets. In particular a greater sample size, a broader range of
590 doses and longer time points after injection will be required to reveal how these effects could be
591 controlled and safely translated into valuable clinical applications of GO based nanovectors for brain
592 diseases.

593

594 **Conclusion**

595 In the present pilot study looking at the acute response to injection of nanovector candidates in the
596 brain, lipid-based NPs, particularly cationic liposomes, induced the greatest inflammatory response in
597 all considered brain regions. In contrast, CNMs were well-tolerated in the brain parenchyma, with
598 assessments at both molecular and histological levels revealing only an acute response at days 1
599 and 2 followed by fast recovery by day 7. No significant differences were observed between the two
600 types of MWNT functionalisation or the two doses of CNMs (1 μg vs 0.5 μg). Among the different
601 CNMs, GO nanosheets displayed the least deleterious profile, with even some beneficial
602 immunomodulatory properties that mitigate the inherent inflammation and brain tissue damages
603 associated with the brain stereotactic administration. Therefore, under the conditions tested here, GO
604 nanosheets appeared to have the best profile for future development as brain nanovector, especially
605 for cerebral applications that require focal drug administration or in conditions with an inherent
606 inflammatory component. Going further, additional investigations should examine not only the long-
607 term fate and chronic effects of these materials after their injection in the brain, but also the long-term
608 consequences of the apparent immunomodulation properties of GO.

609

610 **Experimental Section**

611 **Nanomaterials production**

612 **Functionalised multi-walled carbon nanotubes.** Pristine MWNTs were purchased from
613 Nanostructured and Amorphous Materials Inc. (NanoAmorph, Houston, TX, USA) with a carbon
614 content of 94%. The pristine materials were then modified using either a 1,3-dipolar cycloaddition
615 reaction to obtain aminated MWNTs (MWNT-NH $_3^+$) or a 24-h reaction in H $_2$ SO $_4$ /HNO $_3$ (3:1) solution
616 to produce carboxylated MWNTs (ox-MWNT), as previously described [72, 73].

617

618 **Graphene oxide sheets.** GO flake suspensions in water were prepared from graphite powder
619 (Merck, Sigma-Aldrich, UK) and synthesis was conducted using a modified Hummers' method as
620 previously described [56, 57].

621

622 **Liposomes.** To produce liposomes, 1,2-dioleoyl-3-trimethylammonium-propane hydrochloride
623 (DOTAP) and 1,2-dioleoyl-sn-glycero-3-[phospho-rac-(3-lysyl(1-glycerol))] (DOPG) were kindly
624 provided by Lipoid GmbH (Ludwigshafen, Germany). Cholesterol (CHOL) was purchased from Merck
625 Sigma-Aldrich (UK). Chloroform and methanol were purchased from Thermo Fisher Scientific (UK).
626 Both cationic (DOTAP/CHOL; 2 mM DOTAP:1 mM CHOL) and anionic (DOPG/CHOL; 2 mM
627 DOPG:1 mM CHOL) liposomes were prepared using the film hydration method [74]. Briefly, DOTAP
628 or DOPG and CHOL were dissolved in chloroform/methanol (4:1, v/v) and the organic solvents were
629 evaporated under pressure for 30 min at +40°C using a rotary evaporator. The resulting thin lipid film
630 was hydrated in sterile-filtered 5% (w/v) dextrose solution in water and then bath sonicated for 15 min
631 at +40°C. The final liposome solution was kept at room temperature for 30 min to stabilize the
632 colloidal stability before storage at +4°C for a maximum of 5 days.

633

634 **Characterization of the nanomaterials**

635 **Functionalised multi-walled carbon nanotubes.** MWNTs were analysed by transmission electron
636 microscopy (TEM) to determine the mean diameter and length as previously described for the
637 aminated and carboxylated MWNTs [37, 73]. A Kaiser test was used for MWNT-NH₃⁺ to measure the
638 amount of amine functionalization as previously reported [72]. Kaiser test is based on the colorimetric
639 reaction between the ninhydrin reagent and the amine groups. The reaction gives a blue colour
640 readout and the intensity is proportionally related to the amount of free terminal amine groups [75].
641 DLS was not used to assess hydrodynamic diameter of the GO sheets, as it has been proven non
642 reliable for one dimensional tube-shaped or two-dimensional plate-shaped materials. More systemic
643 characterisation of these materials has been previously reported.

644

645 **Graphene oxide sheets.** GO sheets were characterised by several techniques, including dynamic
646 light scattering (DLS, Nano Zeta Sizer ZS, ZEN3600, Malvern Panalytical, Malvern, UK), TEM
647 (Philips/FEI, Thermo Fisher Scientific, UK), and atomic force microscopy (AFM, Bruker, UK) to
648 assess physicochemical properties. These properties include ζ -potential, lateral dimensions, and the
649 thickness of the sheets. DLS was not used to assess hydrodynamic diameter of the GO sheets, as it
650 has been proven non reliable for two-dimensional plate-shaped or one dimensional tube-shaped
651 materials. More systemic characterisation of these materials were reported previously [57] (in this
652 reference, the GO sheets used herein are named small GO).

653

654 **Liposomes.** Liposomes were first characterised by the DLS technique. Particle diameter and
655 electrophoretic mobility of cationic and anionic liposomes were measured at 25 ± 0.1°C using a Zeta-
656 Sizer unit (Nano Zeta Sizer ZS, ZEN3600, Malvern Panalytical, Malvern, UK). The particle size is
657 based on DLS in back-scattering mode, at 173° and excitation $\lambda=632.8$ nm. For electrophoretic

658 mobility measurements, dispersions were placed into U-shaped cuvettes equipped with gold
659 electrodes. The ζ -potential is related to the electrophoretic mobility by Henry's equation valid in the
660 Smoluchowski approximation, when the screening length is much smaller than the particle radius.
661 The prepared liposomes were also analysed using TEM (Philips/FEI, Thermo Fisher Scientific, UK).

662

663 **Preparation of nanomaterials for brain injection**

664 **Functionalised multi-walled carbon nanotubes.** The day before injection, dry powders of MWNT-
665 NH_3^+ and ox-MWNT were weighed, exposed to low energy UV light for 6 hours in order to "sterilise"
666 the nanotubes, and then rehydrated with sterile-filtered 5% dextrose solution in water (final
667 concentration 1 mg/mL) in sterilised glass container. This material suspension was initially sonicated
668 for 45 min using a water bath sonicator (VWR, UK) operating at 80 W (45 kHz) to allow dispersion of
669 the nanotubes in the dextrose solution. A 0.5 mg/mL suspension was achieved by further dilution in
670 sterile-filtered 5% dextrose solution. All colloidal suspensions kept at +4°C were sonicated for an
671 additional 15 min immediately before the injection.

672

673 **Graphene oxide sheets.** Dry powder of GO sheets that were exposed to UV light for 6 hours after
674 weighting was also rehydrated in sterile-filtered 5% dextrose solution at a concentration of 1 mg/mL.
675 This suspension was sonicated for 30 min using a water bath sonicator (VWR, UK) operating at 80 W
676 (45 kHz) to allow dispersion of GO flakes in the dextrose solution. The 0.5 mg/mL suspension used
677 here was achieved by further dilution in sterile-filtered 5% dextrose solution.

678

679 **Liposomes.** Liposomes were initially prepared at 2 mM DOTAP:1 mM Chol or 2 mM DOPG:1 mM
680 Chol and then further diluted to the final concentration of 1 mg/mL in sterile-filtered 5% dextrose
681 solution.

682

683 The vehicle used for all nanomaterials, sterile-filtered 5% dextrose solution, was used as negative
684 control (*i.e.* basic conditions of inflammation following stereotactic injection of an isotonic solution,
685 such as 5% dextrose in water). Lipopolysaccharide (LPS) O111:B4 suspension at 5 mg/mL in sterile-
686 filtered 5% dextrose solution was used as positive control for inflammatory reaction [37].

687

688 **Animals and sample preparation**

689 A total of 84 young (3-week-old) C57BL/6 male mice were used. The protocol received ethical
690 approval from the University of Manchester under authorisation from the United Kingdom Home
691 Office (project License number PPL-70/7763). Suffering was minimised and the minimal number of
692 animals were used in accordance with the Code of Practice for the housing and care of animals used
693 in scientific procedures. The animals were kept in groups of four to five in standard cages with free
694 access to food and water under controlled environmental conditions, including a 12 h/12 h light/dark
695 cycle.

696

697 For surgery, mice were initially anaesthetised with isoflurane inhalation, injected with analgesic
698 (Buprenorphine 0.1 mg/kg, *im*), and then placed on a stereotactic apparatus. A hole was drilled in the
699 skull at specific lateral coordinates. A total of 1 μ l of the different nanomaterials suspended in 5%
700 dextrose in water was injected in the striatum with a micro-syringe mounted on a stereotaxic holder
701 (coordinates used: lateral (x) -0.1 mm, ventral (y) -2.3 mm, rostro-caudal (z) -3.0 mm from bregma)
702 [76].

703

704 During the surgical procedure, the mice were kept under oxygen and heated using a blanket with a
705 thermostat to maintain body temperature at approximately 37°C. At the end of the procedure, the
706 wound was sutured and the animal was maintained in a thermally controlled incubation chamber at
707 37°C until complete recovery from anaesthesia. The mice were then returned to their maintenance
708 cages and culled at different time points as shown in the experimental design (**Figure 1-A**).

709

710 Mice used for gene expression analyses were sacrificed at 1 day, 2 days, or 7 days after injection (n
711 = 3 per group; total of 63 mice). They were culled with CO₂ exposure followed by cerebral
712 dislocation. The brain was then rapidly dissected out and cut into 2 mm thick slices using a Zivic
713 stainless brain slicer matrix. For each brain, four coronal slices were prepared: one containing the
714 injected area, one immediately posterior to assess diffusion of nanomaterials or of signal in a region
715 adjacent to the injection, and two anterior to the injected area. The most anterior of the latter two
716 slices was used to assess diffusion of nanomaterials or of signal in a distant brain region. From the
717 three brain slices thus sampled, a 2 x 2 x 2 mm tissue block was dissected for RT-qPCR analysis
718 (**Figure 1-A**). In the slice containing the injection site, the sampled tissue block was centred on this
719 site. In the adjacent posterior slice and in the anterior slice, the tissue blocks were sampled along the
720 same antero-posterior and dorso-ventral axes of the injection site. The tissue blocks were snap-
721 frozen in liquid nitrogen and cryopreserved for RNA extraction and real-time RT-qPCR analysis.

722

723 Animals for colorimetric histochemical and immuno-histochemical procedures were sacrificed at day
724 2 after injection (n = 3 per group; total of 21 mice). They were anaesthetised by isoflurane inhalation
725 and then cardiac-perfused with 4% paraformaldehyde in 0.01 M phosphate-buffered saline, pH 7.4
726 (PBS). The brain was then dissected out and immersed overnight in 4% paraformaldehyde in PBS.
727 The following day, brains were soaked in sucrose (5%, 15%, 30% steps) at 4°C for cryoprotection
728 following a previously described procedure [37].

729

730 **Real-Time Quantitative PCR analysis**

731 Tissue blocks from animals injected with GO (0.5 mg/mL), MWNT-NH₃⁺ (0.5 mg/mL), ox-MWNT (0.5
732 mg/mL), cationic liposomes (1 mg/mL), anionic liposomes (1 mg/mL), 5% dextrose (vehicle, negative
733 control), or LPS (positive control) were used for transcript analysis. Tissue blocks were homogenised
734 with a TissueLyser LT (Qiagen, Netherlands) and total RNA was extracted using a NucleoSpin
735 RNA/Protein kit (Macherey-Nagel, Germany) according to the manufacturer's instructions. The
736 concentration of RNA was determined as the optical density ratio 260 nm/280 nm using a

737 BioPhotometer plus (Eppendorf, Germany). Ratio values between 1.8 and 2.2 were considered good
738 quality. Samples of cDNA were prepared from 1 mg RNA in a total volume of 20 μ l using the BioRad
739 iScript cDNA Synthesis Kit (BioRad, USA). Samples were run on a CFX-96 Real Time Detection
740 System (BioRad, USA) with the following sequence: 95°C for 3 min (initial denaturation step), 1
741 cycle; 95°C for 10 sec (amplification), 60°C for 30 sec (annealing), repeated for 40 cycles.
742 Amplification was followed by a melting-curve analysis to confirm PCR product specificity.
743
744 Each RT-PCR reaction in a 25 μ l total volume contained 2 μ l of cDNA from reverse transcription
745 PCR, 12.5 μ l Fast SYBR Green Master Mix (BioRad, UK), and primers at 200 nM each (Merck-
746 Sigma-Aldrich, UK; see **Table S1** for reverse and forward primer sequences). Gene expression
747 levels (*tnf- α* , *il-1 β* , *il-6*, *il-12*, *ifn- γ* , *cxcl10*, *ccl2*, *il-10*, *tgf- β* , *il-4*, and housekeeping gene *β -actin*) were
748 calculated using the Livak method, based on calculation of $2^{-\Delta\Delta CT}$ [77]. *β -actin* was used as a
749 reference housekeeping gene to normalise the amount of target primer transcripts. The normalised
750 values for each gene were compared to the relative expression for 5% dextrose (negative control) to
751 calculate the fold increase of the target gene in the sample.

752

753 **Immuno-histochemical and histochemical procedures**

754 **Tissue processing.** Brains (day 2 post injection) from animals injected with GO (0.5 and 1 mg/mL),
755 MWNT-NH₃⁺ (0.5 and 1 mg/mL), ox-MWNT (0.5 and 1 mg/mL), cationic liposomes (1 mg/mL),
756 anionic liposomes (1 mg/mL), 5% dextrose (vehicle, negative control), or LPS (positive control) were
757 used for cell analyses.

758

759 Following cardiac perfusion of fixative under anaesthesia (as described above), post-fixation, and
760 brain cryoprotection in sucrose, brains were snap-frozen and then cut using a cryo-microtome into
761 30- μ m-thick serial coronal sections. Series of sections (one every 360 μ m) were collected in the
762 following three regions: *i*) anterior to the injection site (from +1.9 to +1.0 from bregma), *ii*) at the
763 injection site (from -0.1 to -0.9 from bregma), and *iii*) posterior to it (from -1.2 to -2.0 from bregma).

764

765 **Immuno-phenotyping of neurons, microglia, astrocytes, and apoptotic cells.** For each
766 experimental group ($n = 3$ animals per group), a series of sections was processed for immuno-
767 histochemistry. Free-floating sections were pre-treated with 1% H₂O₂ (Merck Sigma-Aldrich, UK) for
768 15 sec at room temperature, rinsed in PBS (Merck Sigma-Aldrich, UK), and incubated in 5% Normal
769 Serum of the appropriate species (Vector Lab, USA; **Table S2**), and 0.03% Triton-X100 (Merck
770 Sigma-Aldrich, UK) in PBS for 1 h at room temperature to prevent nonspecific binding. After rinsing in
771 PBS, the sections were incubated overnight at 4°C in primary antibodies (**Table S2**) diluted in 1%
772 Normal Serum in PBS. The sections were then incubated in biotinylated secondary antibodies
773 (Vector Lab) in 1% Normal Serum in PBS. The sections were then reacted with the Vectastain ABC
774 kit (Vector Lab) and finally with 0.5% 3-3' diaminobenzidine (DAB, Merck-Sigma-Aldrich) in PBS.
775 After rinsing, the sections were dehydrated through an increasing alcohol gradient, mounted, and

776 cover-slipped. The sections were examined with an Olympus microscope equipped with a QICAM
777 digital camera (QImaging, Canada) using Image-Pro Plus 7.0 Software (Media Cybernetics, USA).
778

779 **Fluoro-Jade B histochemistry.** To evaluate ongoing neuronal cell death, Fluoro-Jade B staining
780 was performed [60]. Sections were mounted on gelatin-coated slides, air dried, and soaked for 5 min
781 in 1% NaOH (Merck-Sigma-Aldrich) in 80% alcohol in distilled water. The sections were then soaked
782 for 2 min in 70% alcohol and 2 min in distilled water, and then in a solution of 0.06% potassium
783 permanganate (Merck Sigma-Aldrich) for 10 min to reduce the background signal. The sections were
784 then rinsed in distilled water for 2 min and soaked for 15 min in the staining solution. The Fluoro-Jade
785 B working solution (0.0004%) was obtained by diluting 4 mL of 0.01% stock solution (10 mg of
786 powder [Histochem Inc., USA] in 100 mL of distilled water) into 96 mL of 0.1% acetic acid (Merck
787 Sigma-Aldrich). The sections were then rinsed in distilled water and air dried. They were cleared in
788 xylene for 2 min, mounted, and then cover-slipped. The sections were analysed with an Olympus
789 microscope equipped with a UV bulb light source (450-490 nm blue excitation light filter; Fluoro-Jade
790 B has a green light emission) and images were taken with a QICAM digital camera (QImaging,
791 Surrey, BC, Canada).
792

793 **Quantitative analyses**

794 **Counts of neurons and astrocytes.** To assess whether the intra-striatal injection of nanomaterials
795 induced neuronal cell loss, the number of neurons identified by NeuN immunoreactivity was
796 estimated using a stereological approach in all groups of mice (animals sacrificed at day 2 after
797 injection of all the materials; $n = 3$ per group; total of 21 mice).
798

799 Stereology was also used to estimate the number of astrocytes. This was based on glial fibrillary
800 acidic protein (GFAP) immunostaining in the mice treated with 5% dextrose, LPS, or cationic
801 liposomes. Cell counting was performed using three regions of interest (ROIs) per section in six
802 sections (2 regularly spaced sections through the anterior region, the injection site, and the posterior
803 region, respectively) per mouse and three mice per group. The counting of astrocytes was performed
804 in three ROIs per section in six sections sampled as above per mouse and three mice per group.
805 Sections were analysed with an Olympus microscope equipped with a Retiga-2000R CCD Camera
806 (QImaging, Canada) and counting was performed with the Optical Fractionator probe included in
807 Stereo Investigator 10 software (MBF Bioscience, USA).
808

809 **Analysis of glial cell coverage and optical density of microglial cells.** A series of sections for
810 each condition ($n = 3$; immunostained as described above for visualisation of microglial cells and
811 astrocytes) were used to assess the percentage of the area covered by CD11b- and GFAP-immuno-
812 positive cells, assuming that a larger area is covered by activated glial cells than by “resting” cells
813 [78, 79]. The immunostaining was thus quantified as the percentage of the total image area,
814 considering the site of injection in the striatum and an equivalent ROI in the anterior and posterior
815 sections.

816

817 The intensity of the CD11b immunoreactivity was also quantified by densitometry. A quantitative
818 densitometric analysis [80-82] was performed to measure (in the same sections) the intensity of
819 immunoreactivity signal in the cell somata [83]. For this analysis, three ROIs (with an area of 289
820 μm^2) per section in six sections per mouse sampled as above and in three mice per group were
821 used. Sections were analysed with an Olympus microscope and 8-bit grey-scale images were taken
822 with a 20X objective and a QImaging QICAM digital camera (QImaging, Canada) maintaining
823 constant light conditions and magnification. Images were then processed using the Image-Pro Plus
824 7.0 software (Media Cybernetics, USA). A signal from non-immunostained tissue (contralateral
825 hemisphere) was used to subtract the background signal.

826

827 **Statistics**

828 The results were expressed as mean per group \pm standard error of the mean (SEM). The Livak
829 method was used to analyse qPCR data using ΔCT values [77]. Data were checked for normal
830 distribution before running statistical analysis. Statistical variations were evaluated as follows: for
831 simple comparisons unpaired t-tests were used and one-way analysis of variance (ANOVA) per
832 group, followed by Bonferroni *post-hoc* for testing pairwise comparisons. For immuno-histochemical
833 and histochemical analysis, the number of sample units used in each study group (n=3) has been
834 compensated by different measures of the parameter (3 different ROIs) in the areas of interest, within
835 the brain (anterior site, injection site, and posterior site). GraphPad Prism (GraphPad Software v.6)
836 was used for statistical analyses. p-values < 0.05 were considered significant.

837

838 **Supporting Information**

839 Supporting Information is available from the Wiley Online Library or from the author.

840 *Pdf document attached.*

841

842 **Funding**

843 This work was partly supported by the EU H2020 RTD Framework Program: FET Graphene Flagship
844 project (H2020-EU.1.2.3.- FET Flagships; GrapheneCore; 2785219), the Centre National de la
845 Recherche Scientifique (CNRS), the International Center for Frontier Research in Chemistry (icFRC),
846 and the Agence Nationale de la Recherche (ANR) through the LabEx project Chemistry of Complex
847 Systems (ANR-10-LABX-0026_CSC). Financial support to this project was partially provided by The
848 Fondazione Cariverona ("*Verona Nanomedicine Initiative*") and funding from an intramural (University
849 of Verona) international cooperation program ("*CooperInt*") was obtained. KK would like to
850 acknowledge the Severo Ochoa Centre of Excellence Award to ICN2.

851

852

853

854 **Authors' contributions**

855 C.P., C.B., and K.K. conceived the overall design of the project with contributions from A.B and M.P.
856 to the planning of the experiments. C.P. and C.B. implemented the experiments and analyzed the
857 data under the supervision of C.B., K.K., and M.B., with contributions from M.M., D.A.J., and N.L.
858 D.A.J. prepared the GO sheets and N.L. prepared the liposomes. A.B. and M.P. produced and
859 characterized the functionalised carbon nanotubes. C.P. and C.B. wrote the manuscript draft. All
860 authors discussed the results, contributed to the writing and critical revision of the article, and
861 approved the version to be published.

862

863 **Acknowledgments**

864 The authors would like to thank Dr Irene de Lázaro for fruitful discussion regarding statistical
865 analyses of the RT-qPCR data, Ms Lana Papafilippou for the TEM imaging of the cationic liposomes,
866 and Dr Marco Sandri (Big and Open Data Innovation Laboratory - BODaI-Lab, University of Brescia,
867 Italy) for the valuable scientific support in the biostatistical analysis of the data. Graphical abstract
868 and Figure 1A were created using BioRender.com.

869

870 **Data Availability**

871 The raw/processed data required to reproduce these findings cannot be shared at this time as the
872 data also forms part of an ongoing study.

873

874 **References**

- 875 [1] D. Furtado, M. Bjornmalm, S. Ayton, A.I. Bush, K. Kempe, F. Caruso, 2018. Overcoming the
876 blood-brain barrier: The role of nanomaterials in treating neurological diseases. *Adv Mater.* 30,
877 e1801362. <https://doi.org/10.1002/adma.201801362>.
- 878 [2] Y. Cheng, R.A. Morshed, B. Auffinger, A.L. Tobias, M.S. Lesniak, Multifunctional nanoparticles for
879 brain tumor imaging and therapy, *Adv Drug Deliv Rev.* 66 (2014) 42-57.
880 <https://doi.org/10.1016/j.addr.2013.09.006>
- 881 [3] L. Biddlestone-Thorpe, N. Marchi, K. Guo, C. Ghosh, D. Janigro, K. Valerie, H. Yang,
882 Nanomaterial-mediated cns delivery of diagnostic and therapeutic agents, *Adv Drug Deliv Rev.* 64
883 (2012) 605-613. <https://doi.org/10.1016/j.addr.2011.11.014>.
- 884 [4] A. Dominguez, B. Suarez-Merino, F. Goni-de-Cerio, Nanoparticles and blood-brain barrier: The
885 key to central nervous system diseases, *J Nanosci Nanotechnol.* 14 (2014) 766-779.
886 <https://doi.org/10.1166/jnn.2014.9119>.
- 887 [5] G. Modi, V. Pillay, Y.E. Choonara, V.M. Ndesendo, L.C. du Toit, D. Naidoo, Nanotechnological
888 applications for the treatment of neurodegenerative disorders, *Prog Neurobiol.* 88 (2009) 272-285.
889 <https://doi.org/10.1016/j.pneurobio.2009.05.002>.
- 890 [6] M. Caffo, L. Merlo, D. Marino, G. Caruso, Graphene in neurosurgery: The beginning of a new era,
891 *Nanomedicine (Lond).* 10 (2015) 615-625. <https://doi.org/10.2217/nnm.14.195>.
- 892 [7] J.T. Wang, K.T. Al-Jamal, Functionalized carbon nanotubes: Revolution in brain delivery,
893 *Nanomedicine (Lond).* 10 (2015) 2639-2642. [10.2217/nnm.15.114](https://doi.org/10.2217/nnm.15.114).
- 894 [8] H. Kafa, J.T. Wang, K.T. Al-Jamal, Current perspective of carbon nanotubes application in
895 neurology, *Int Rev Neurobiol.* 130 (2016) 229-263. <https://doi.org/10.1016/bs.irm.2016.07.001>.
- 896 [9] B.S. Wong, S.L. Yoong, A. Jagusiak, T. Panczyk, H.K. Ho, W.H. Ang, G. Pastorin, Carbon
897 nanotubes for delivery of small molecule drugs, *Adv Drug Deliv Rev.* 65 (2013) 1964-2015.
898 <https://doi.org/10.1016/j.addr.2013.08.005>.

899 [10] M. Bramini, G. Alberini, E. Colombo, M. Chiacchiaretta, M.L. DiFrancesco, J.F. Maya-
900 Vetencourt, L. Maragliano, F. Benfenati, F. Cesca, Interfacing graphene-based materials with neural
901 cells, *Front Syst Neurosci.* 12 (2018) 12. <https://doi.org/10.3389/fnsys.2018.00012>.

902 [11] A. Bianco, K. Kostarelos, C.D. Partidos, M. Prato, Biomedical applications of functionalised
903 carbon nanotubes, *Chem Commun (Camb).* 5 (2005) 571-577. <https://doi.org/10.1039/b410943k>.

904 [12] A. Bianco, K. Kostarelos, M. Prato, Applications of carbon nanotubes in drug delivery, *Curr Opin*
905 *Chem Biol.* 9 (2005) 674-679. <https://doi.org/10.1016/j.cbpa.2005.10.005>.

906 [13] L. Lacerda, A. Bianco, M. Prato, K. Kostarelos, Carbon nanotubes as nanomedicines: From
907 toxicology to pharmacology, *Adv Drug Deliv Rev.* 58 (2006) 1460-1470.
908 <https://doi.org/10.1016/j.addr.2006.09.015>.

909 [14] K. Kostarelos, K.S. Novoselov, Graphene devices for life, *Nat Nanotechnol.* 9 (2014) 744-745.
910 <https://doi.org/10.1038/nnano.2014.224>.

911 [15] T.A. Mattei, How graphene is expected to impact neurotherapeutics in the near future, *Expert*
912 *Rev Neurother.* 14 (2014) 845-847. <https://doi.org/10.1586/14737175.2014.925804>.

913 [16] X. Guo, N. Mei, Assessment of the toxic potential of graphene family nanomaterials, *J Food*
914 *Drug Anal.* 22 (2014) 105-115. <https://doi.org/10.1016/j.jfda.2014.01.009>.

915 [17] K. Zhou, G.A. Thouas, C.C. Bernard, D.R. Nisbet, D.I. Finkelstein, D. Li, J.S. Forsythe, Method
916 to impart electro- and biofunctionality to neural scaffolds using graphene-polyelectrolyte multilayers,
917 *ACS Appl Mater Interfaces.* 4 (2012) 4524-4531. <https://doi.org/10.1021/am3007565>.

918 [18] S.M. Chowdhury, C. Surhland, Z. Sanchez, P. Chaudhary, M.A. Suresh Kumar, S. Lee, L.A.
919 Pena, M. Waring, B. Sitharaman, M. Naidu, Graphene nanoribbons as a drug delivery agent for
920 lucanthone mediated therapy of glioblastoma multiforme, *Nanomedicine.* 11 (2015) 109-118.
921 <https://doi.org/10.1016/j.nano.2014.08.001>.

922 [19] J. Ren, S. Shen, D. Wang, Z. Xi, L. Guo, Z. Pang, Y. Qian, X. Sun, X. Jiang, The targeted
923 delivery of anticancer drugs to brain glioma by pegylated oxidized multi-walled carbon nanotubes
924 modified with angiopep-2, *Biomaterials.* 33 (2012) 3324-3333.
925 <https://doi.org/10.1016/j.biomaterials.2012.01.025>.

926 [20] M.K. Gottipati, E. Bekyarova, R.C. Haddon, V. Parpura, Chemically functionalized single-walled
927 carbon nanotubes enhance the glutamate uptake characteristics of mouse cortical astrocytes, *Amino*
928 *Acids.* 47 (2015) 1379-1388. <https://doi.org/10.1007/s00726-015-1970-9>.

929 [21] X. Xue, L.R. Wang, Y. Sato, Y. Jiang, M. Berg, D.S. Yang, R.A. Nixon, X.J. Liang, Single-walled
930 carbon nanotubes alleviate autophagic/lysosomal defects in primary glia from a mouse model of
931 alzheimer's disease, *Nano Lett.* 14 (2014) 5110-5117. <https://doi.org/10.1021/nl501839q>.

932 [22] K.T. Al-Jamal, L. Gherardini, G. Bardi, A. Nunes, C. Guo, C. Bussy, M.A. Herrero, A. Bianco, M.
933 Prato, K. Kostarelos, T. Pizzorusso, Functional motor recovery from brain ischemic insult by carbon
934 nanotube-mediated sirna silencing, *Proc Natl Acad Sci USA.* 108 (2011) 10952-10957.
935 <https://doi.org/10.1073/pnas.1100930108>.

936 [23] Z. Yang, Y. Zhang, Y. Yang, L. Sun, D. Han, H. Li, C. Wang, Pharmacological and toxicological
937 target organelles and safe use of single-walled carbon nanotubes as drug carriers in treating
938 alzheimer disease, *Nanomedicine.* 6 (2010) 427-441. <https://doi.org/10.1016/j.nano.2009.11.007>.

939 [24] H. Kafa, J.T. Wang, N. Rubio, K. Venner, G. Anderson, E. Pach, B. Ballesteros, J.E. Preston,
940 N.J. Abbott, K.T. Al-Jamal, The interaction of carbon nanotubes with an in vitro blood-brain barrier
941 model and mouse brain in vivo, *Biomaterials.* 53 (2015) 437-452.
942 <https://doi.org/10.1016/j.biomaterials.2015.02.083>.

943 [25] S. Shityakov, E. Salvador, G. Pastorin, C. Forster, Blood-brain barrier transport studies,
944 aggregation, and molecular dynamics simulation of multiwalled carbon nanotube functionalized with
945 fluorescein isothiocyanate, *Int J Nanomedicine.* 10 (2015) 1703-1713.
946 <https://doi.org/10.2147/IJN.S68429>.

947 [26] H. Kafa, J.T. Wang, N. Rubio, R. Klippstein, P.M. Costa, H.A. Hassan, J.K. Sosabowski, S.S.
948 Bansal, J.E. Preston, N.J. Abbott, K.T. Al-Jamal, Translocation of Irf1 targeted carbon nanotubes of
949 different diameters across the blood-brain barrier in vitro and in vivo, *J Control Release.* 225 (2016)
950 217-229. <https://doi.org/10.1016/j.jconrel.2016.01.031>.

951 [27] J.T. Wang, N. Rubio, H. Kafa, E. Venturelli, C. Fabbro, C. Menard-Moyon, T. Da Ros, J.K.
952 Sosabowski, A.D. Lawson, M.K. Robinson, M. Prato, A. Bianco, F. Festy, J.E. Preston, K.
953 Kostarelos, K.T. Al-Jamal, Kinetics of functionalised carbon nanotube distribution in mouse brain
954 after systemic injection: Spatial to ultra-structural analyses, *J Control Release.* 224 (2016) 22-32.
955 <https://doi.org/10.1016/j.jconrel.2015.12.039>.

956 [28] Y. Liu, L.P. Xu, W. Dai, H. Dong, Y. Wen, X. Zhang, Graphene quantum dots for the inhibition of
957 beta amyloid aggregation, *Nanoscale.* 7 (2015) 19060-19065. <https://doi.org/10.1039/c5nr06282a>.

958 [29] M. Li, X. Yang, J. Ren, K. Qu, X. Qu, Using graphene oxide high near-infrared absorbance for
959 photothermal treatment of alzheimer's disease, *Adv Mater.* 24 (2012) 1722-1728.
960 10.1002/adma.201104864.

961 [30] L. Feng, L. Wu, X. Qu, New horizons for diagnostics and therapeutic applications of graphene
962 and graphene oxide, *Adv Mater.* 25 (2013) 168-186. 10.1002/adma.201203229.

963 [31] G. Liu, H. Shen, J. Mao, L. Zhang, Z. Jiang, T. Sun, Q. Lan, Z. Zhang, Transferrin modified
964 graphene oxide for glioma-targeted drug delivery: In vitro and in vivo evaluations, *ACS Appl Mater*
965 *Interfaces.* 5 (2013) 6909-6914. <https://doi.org/10.1021/am402128s>.

966 [32] Y. Kang, J. Liu, S. Yin, Y. Jiang, X. Feng, J. Wu, Y. Zhang, A. Chen, Y. Zhang, L. Shao,
967 Oxidation of reduced graphene oxide via cellular redox signaling modulates actin-mediated
968 neurotransmission, *ACS NANO.* (2020). 10.1021/acsnano.9b08078.

969 [33] H. Peluffo, U. Unzueta, M.L. Negro-Demontel, Z. Xu, E. Vaquez, N. Ferrer-Miralles, A.
970 Villaverde, Bbb-targeting, protein-based nanomedicines for drug and nucleic acid delivery to the cns,
971 *Biotechnol Adv.* 33 (2015) 277-287. <https://doi.org/10.1016/j.biotechadv.2015.02.004>

972 [34] M.W. Salter, B. Stevens, Microglia emerge as central players in brain disease, *Nat Med.* 23
973 (2017) 1018-1027. <https://doi.org/10.1038/nm.4397>.

974 [35] M. Bentivoglio, R. Mariotti, G. Bertini, Neuroinflammation and brain infections: Historical context
975 and current perspectives, *Brain Res Rev.* 66 (2011) 152-173.
976 <https://doi.org/10.1016/j.brainresrev.2010.09.008>.

977 [36] G. Bardi, P. Tognini, G. Ciofani, V. Raffa, M. Costa, T. Pizzorusso, Pluronic-coated carbon
978 nanotubes do not induce degeneration of cortical neurons in vivo and in vitro, *Nanomedicine.* 5
979 (2009) 96-104. <https://doi.org/10.1016/j.nano.2008.06.008>.

980 [37] G. Bardi, A. Nunes, L. Gherardini, K. Bates, K.T. Al-Jamal, C. Gaillard, M. Prato, A. Bianco, T.
981 Pizzorusso, K. Kostarelos, 2013. Functionalized carbon nanotubes in the brain: Cellular
982 internalization and neuroinflammatory responses. *PLoS One.* 8, e80964.
983 <https://doi.org/10.1371/journal.pone.0080964>.

984 [38] L. Dal Bosco, G.E. Weber, G.M. Parfitt, K. Paese, C.O. Goncalves, T.M. Serodre, C.A. Furtado,
985 A.P. Santos, J.M. Monserrat, D.M. Barros, Pegylated carbon nanotubes impair retrieval of contextual
986 fear memory and alter oxidative stress parameters in the rat hippocampus, *Biomed Res Int.* 2015
987 (2015) 1-11. <https://doi.org/10.1155/2015/104135>.

988 [39] L. Dal Bosco, G.E. Weber, G.M. Parfitt, A.P. Cordeiro, S.K. Sahoo, C. Fantini, M.C. Klosterhoff,
989 L.A. Romano, C.A. Furtado, A.P. Santos, J.M. Monserrat, D.M. Barros, 2015. Biopersistence of
990 pegylated carbon nanotubes promotes a delayed antioxidant response after infusion into the rat
991 hippocampus. *PLoS One.* 10, e0129156. <https://doi.org/10.1371/journal.pone.0129156>.

992 [40] C. Bussy, K.T. Al-Jamal, J. Boczkowski, S. Lanone, M. Prato, A. Bianco, K. Kostarelos, Microglia
993 determine brain region-specific neurotoxic responses to chemically functionalized carbon nanotubes,
994 *ACS NANO.* 9 (2015) 7815-7830. <https://doi.org/10.1021/acsnano.5b02358>.

995 [41] L. Yang, F. Wang, H. Han, L. Yang, G. Zhang, Z. Fan, Functionalized graphene oxide as a drug
996 carrier for loading pirfenidone in treatment of subarachnoid hemorrhage, *Colloids Surf B*
997 *Biointerfaces.* 129 (2015) 21-29. <https://doi.org/10.1016/j.colsurfb.2015.03.022>.

998 [42] R. Rauti, N. Lozano, V. Leon, D. Scaini, M. Musto, I. Rago, F.P. Ulloa Severino, A. Fabbro, L.
999 Casalis, E. Vazquez, K. Kostarelos, M. Prato, L. Ballerini, Graphene oxide nanosheets reshape
1000 synaptic function in cultured brain networks, *ACS NANO.* 10 (2016) 4459-4471.
1001 <https://doi.org/10.1021/acsnano.6b00130>.

1002 [43] M. Bramini, S. Sacchetti, A. Armirotti, A. Rocchi, E. Vazquez, V. Leon Castellanos, T. Bandiera,
1003 F. Cesca, F. Benfenati, Graphene oxide nanosheets disrupt lipid composition, ca(2+) homeostasis,
1004 and synaptic transmission in primary cortical neurons, *ACS NANO.* 10 (2016) 7154-7171.
1005 <https://doi.org/10.1021/acsnano.6b03438>.

1006 [44] M. Chiacchiarretta, M. Bramini, A. Rocchi, A. Armirotti, E. Giordano, E. Vazquez, T. Bandiera, S.
1007 Ferroni, F. Cesca, F. Benfenati, Graphene oxide upregulates the homeostatic functions of primary
1008 astrocytes and modulates astrocyte-to-neuron communication, *Nano Lett.* (2018).
1009 <https://doi.org/10.1021/acs.nanolett.8b02487>.

1010 [45] C. Hoyle, J. Rivers-Auty, E. Lemarchand, S. Vranic, E. Wang, M. Buggio, N.J. Rothwell, S.M.
1011 Allan, K. Kostarelos, D. Brough, Small, thin graphene oxide is anti-inflammatory activating nuclear
1012 factor erythroid 2-related factor 2 via metabolic reprogramming, *ACS NANO.* 12 (2018) 11949-11962.
1013 <https://doi.org/10.1021/acsnano.8b03642>.

1014 [46] H. Lv, S. Zhang, B. Wang, S. Cui, J. Yan, Toxicity of cationic lipids and cationic polymers in gene
1015 delivery, *J Control Release.* 114 (2006) 100-109. <https://doi.org/10.1016/j.jconrel.2006.04.014>.

1016 [47] M.C. Fillion, N.C. Phillips, Toxicity and immunomodulatory activity of liposomal vectors
1017 formulated with cationic lipids toward immune effector cells, *Biochim Biophys Acta.* 1329 (1997) 345-
1018 356. [https://doi.org/10.1016/S0005-2736\(97\)00126-0](https://doi.org/10.1016/S0005-2736(97)00126-0).
1019 [48] K.B. Knudsen, H. Northeved, P.K. Ek, A. Permin, T.L. Andresen, S. Larsen, K.M. Wegener, H.R.
1020 Lam, J. Lykkesfeldt, Differential toxicological response to positively and negatively charged
1021 nanoparticles in the rat brain, *Nanotoxicology.* 8 (2014) 764-774.
1022 <https://doi.org/10.3109/17435390.2013.829589>.
1023 [49] K.B. Knudsen, H. Northeved, P.E. Kumar, A. Permin, T. Gjetting, T.L. Andresen, S. Larsen, K.M.
1024 Wegener, J. Lykkesfeldt, K. Jantzen, S. Loft, P. Moller, M. Roursgaard, In vivo toxicity of cationic
1025 micelles and liposomes, *Nanomedicine.* 11 (2015) 467-477.
1026 <https://doi.org/10.1016/j.nano.2014.08.004>.
1027 [50] R. Rauti, M. Medelin, L. Newman, S. Vranic, G. Reina, A. Bianco, M. Prato, K. Kostarelos, L.
1028 Ballerini, Graphene oxide flakes tune excitatory neurotransmission in vivo by targeting hippocampal
1029 synapses, *Nano Lett.* 19 (2019) 2858-2870. [10.1021/acs.nanolett.8b04903](https://doi.org/10.1021/acs.nanolett.8b04903).
1030 [51] C. Klumpp, K. Kostarelos, M. Prato, A. Bianco, Functionalized carbon nanotubes as emerging
1031 nanovectors for the delivery of therapeutics, *Biochim Biophys Acta.* 1758 (2006) 404-412.
1032 [10.1016/j.bbame.2005.10.008](https://doi.org/10.1016/j.bbame.2005.10.008).
1033 [52] A. Bianco, K. Kostarelos, M. Prato, Making carbon nanotubes biocompatible and biodegradable,
1034 *Chem Commun* 47 (2011) 10182-10188. [10.1039/c1cc13011k](https://doi.org/10.1039/c1cc13011k).
1035 [53] A. Nunes, C. Bussy, L. Gherardini, M. Meneghetti, M.A. Herrero, A. Bianco, M. Prato, T.
1036 Pizzorusso, K.T. Al-Jamal, K. Kostarelos, *In vivo* degradation of functionalized carbon nanotubes
1037 after stereotactic administration in the brain cortex, *Nanomedicine (Lond).* 7 (2012) 1485-1494.
1038 <https://doi.org/10.2217/nnm.12.33>.
1039 [54] A. Nunes, K. Al-Jamal, T. Nakajima, M. Hariz, K. Kostarelos, Application of carbon nanotubes in
1040 neurology: Clinical perspectives and toxicological risks, *Arch Toxicol.* 86 (2012) 1009-1020.
1041 <https://doi.org/10.1007/s00204-012-0860-0>.
1042 [55] C. Bussy, C. Hadad, M. Prato, A. Bianco, K. Kostarelos, Intracellular degradation of chemically
1043 functionalized carbon nanotubes using a long-term primary microglial culture model, *Nanoscale.* 8
1044 (2016) 590-601. [10.1039/c5nr06625e](https://doi.org/10.1039/c5nr06625e).
1045 [56] A.D. Jasim, N. Lozano, K. Kostarelos, 2016. Synthesis of few-layered, high-purity graphene
1046 oxide sheets from different graphite sources for biology. *2D materials.* 3, 014006.
1047 <https://doi.org/10.1088/2053-1583/3/1/014006>.
1048 [57] A.F. Rodrigues, L. Newman, N. Lozano, S.P. Mukherjee, B. Fadeel, C. Bussy, K. Kostarelos,
1049 2018. A blueprint for the synthesis and characterisation of thin graphene oxide with controlled lateral
1050 dimensions for biomedicine. *2D materials.* 5, 035020. <https://doi.org/10.1088/2053-1583/aac05c>.
1051 [58] C. Mamot, J.B. Nguyen, M. Pourdehnad, P. Hadaczek, R. Saito, J.R. Bringas, D.C. Drummond,
1052 K. Hong, D.B. Kirpotin, T. McKnight, M.S. Berger, J.W. Park, K.S. Bankiewicz, Extensive distribution
1053 of liposomes in rodent brains and brain tumors following convection-enhanced delivery, *J*
1054 *Neurooncol.* 68 (2004) 1-9. <https://doi.org/10.1023/B:NEON.0000024743.56415.4b>.
1055 [59] L. Gallentoft, L.M. Pettersson, N. Danielsen, J. Schouenborg, C.N. Prinz, C.E. Linsmeier, Size-
1056 dependent long-term tissue response to biostable nanowires in the brain, *Biomaterials.* 42 (2015)
1057 172-183. <https://doi.org/10.1016/j.biomaterials.2014.11.051>.
1058 [60] L.C. Schmued, K.J. Hopkins, Fluoro-jade b: A high affinity fluorescent marker for the localization
1059 of neuronal degeneration, *Brain Res.* 874 (2000) 123-130. [https://doi.org/10.1016/S0006-
1060 8993\(00\)02513-0](https://doi.org/10.1016/S0006-8993(00)02513-0).
1061 [61] V. Mirshafiee, W. Jiang, B. Sun, X. Wang, T. Xia, Facilitating translational nanomedicine via
1062 predictive safety assessment, *Mol Ther.* 25 (2017) 1522-1530.
1063 <https://doi.org/10.1016/j.ymthe.2017.03.011>.
1064 [62] P. Møller, J. Lykkesfeldt, Positive charge, negative effect: The impact of cationic nanoparticles in
1065 the brain, *Nanomedicine (Lond).* 9 (2014) 1441-1443. <https://doi.org/10.2217/nnm.14.91>.
1066 [63] M.L. Immordino, F. Dosio, L. Cattel, Stealth liposomes: Review of the basic science, rationale,
1067 and clinical applications, existing and potential, *Int J Nanomedicine.* 1 (2006) 297-315. 2426795
1068 [64] M. Simard, M. Nedergaard, The neurobiology of glia in the context of water and ion homeostasis,
1069 *Neuroscience.* 129 (2004) 877-896. <https://doi.org/10.1016/j.neuroscience.2004.09.053>.
1070 [65] M.V. Sofroniew, H.V. Vinters, Astrocytes: Biology and pathology, *Acta Neuropathol.* 119 (2010)
1071 7-35. <https://doi.org/10.1007/s00401-009-0619-8>.
1072 [66] M.L. Block, L. Zecca, J.S. Hong, Microglia-mediated neurotoxicity: Uncovering the molecular
1073 mechanisms, *Nat Rev Neurosci.* 8 (2007) 57-69. <https://doi.org/10.1038/nrn2038>.
1074 [67] S.J. Soenen, E. Illyes, D. Vercauteren, K. Braeckmans, Z. Majer, S.C. De Smedt, M. De Cuyper,
1075 The role of nanoparticle concentration-dependent induction of cellular stress in the internalization of

1076 non-toxic cationic magnetoliposomes, *Biomaterials*. 30 (2009) 6803-6813.
1077 <https://doi.org/10.1016/j.biomaterials.2009.08.050>.
1078 [68] R. Banerjee, Liposomes: Applications in medicine, *J Biomater Appl*. 16 (2001) 3-21.
1079 <https://doi.org/10.1106/RA7U-1V9C-RV7C-8QXL>.
1080 [69] B. Fadeel, C. Bussy, S. Merino, E. Vazquez, E. Flahaut, F. Mouchet, L. Evariste, L. Gauthier,
1081 A.J. Koivisto, U. Vogel, C. Martin, L.G. Delogu, T. Buerki-Thurnherr, P. Wick, D. Beloin-Saint-Pierre,
1082 R. Hischier, M. Pelin, F. Candotto Carniel, M. Tretiach, F. Cesca, F. Benfenati, D. Scaini, L. Ballerini,
1083 K. Kostarelos, M. Prato, A. Bianco, Safety assessment of graphene-based materials: Focus on
1084 human health and the environment, *ACS NANO*. 12 (2018) 10582-10620.
1085 <https://doi.org/10.1021/acsnano.8b04758>.
1086 [70] C. Bussy, H. Ali-Boucetta, K. Kostarelos, Safety considerations for graphene: Lessons learnt
1087 from carbon nanotubes, *Acc Chem Res*. 46 (2013) 692-701. 10.1021/ar300199e.
1088 [71] M. Rezazadeh Azari, Y. Mohammadian, Comparing in vitro cytotoxicity of graphite, short multi-
1089 walled carbon nanotubes, and long multi-walled carbon nanotubes, *Environ Sci Pollut Res Int*.
1090 (2020). 10.1007/s11356-020-08036-4.
1091 [72] V. Georgakilas, N. Tagmatarchis, D. Pantarotto, A. Bianco, J.P. Briand, M. Prato, Amino acid
1092 functionalisation of water soluble carbon nanotubes, *Chem Commun (Camb)*. (2002) 3050-3051.
1093 <https://doi.org/10.1039/b209843a>.
1094 [73] S. Li, W. Wu, S. Campidelli, V. Sarnatskaia, M. Prato, A. Tridon, A. Nikolaev, V. Nikolaev, A.
1095 Bianco, E. Snezhkova, Adsorption of carbon nanotubes on active carbon microparticles, *Carbon*. 46
1096 (2008) 1091-1095. <https://doi.org/10.1016/j.carbon.2008.03.010>.
1097 [74] N. Lozano, W.T. Al-Jamal, A. Taruttis, N. Beziere, N.C. Burton, J. Van den Bossche, M. Mazza,
1098 E. Herzog, V. Ntziachristos, K. Kostarelos, Liposome-gold nanorod hybrids for high-resolution
1099 visualization deep in tissues, *J Am Chem Soc*. 134 (2012) 13256-13258.
1100 <https://doi.org/10.1021/ja304499q>.
1101 [75] E. Kaiser, R.L. Colescott, C.D. Bossinger, P.I. Cook, Color test for detection of free terminal
1102 amino groups in the solid-phase synthesis of peptides, *Anal Biochem*. 34 (1970) 595-598.
1103 10.1016/0003-2697(70)90146-6.
1104 [76] G. Paxinos, K. Franklin, Paxinos and franklin's the mouse brain in stereotaxic coordinates, ed,
1105 2012
1106 [77] K.J. Livak, T.D. Schmittgen, Analysis of relative gene expression data using real-time
1107 quantitative pcr and the 2(-delta delta c(t)) method, *Methods*. 25 (2001) 402-408.
1108 <https://doi.org/10.1006/meth.2001.1262>.
1109 [78] H. Dou, K. Birusingh, J. Faraci, S. Gorantla, L.Y. Poluektova, S.B. Maggirwar, S. Dewhurst, H.A.
1110 Gelbard, H.E. Gendelman, Neuroprotective activities of sodium valproate in a murine model of
1111 human immunodeficiency virus-1 encephalitis, *J Neurosci*. 23 (2003) 9162-9170.
1112 <https://doi.org/10.1523/JNEUROSCI.23-27-09162.2003>.
1113 [79] H. Dou, J. Morehead, J. Bradley, S. Gorantla, B. Ellison, J. Kingsley, L.M. Smith, W. Chao, G.
1114 Bentsman, D.J. Volsky, H.E. Gendelman, Neuropathologic and neuroinflammatory activities of hiv-1-
1115 infected human astrocytes in murine brain, *Glia*. 54 (2006) 81-93. <https://doi.org/10.1002/glia.20358>.
1116 [80] A.C. Ferraz, L.L. Xavier, S. Hernandez, M. Sulzbach, G.G. Viola, J.A. Anselmo-Franci, M.
1117 Achaval, C. Da Cunha, Failure of estrogen to protect the substantia nigra pars compacta of female
1118 rats from lesion induced by 6-hydroxydopamine, *Brain Res*. 986 (2003) 200-205.
1119 [https://doi.org/10.1016/s0006-8993\(03\)03198-6](https://doi.org/10.1016/s0006-8993(03)03198-6).
1120 [81] L.L. Xavier, G.G. Viola, A.C. Ferraz, C. Da Cunha, J.M. Deonizio, C.A. Netto, M. Achaval, A
1121 simple and fast densitometric method for the analysis of tyrosine hydroxylase immunoreactivity in the
1122 substantia nigra pars compacta and in the ventral tegmental area, *Brain Res Brain Res Protoc*. 16
1123 (2005) 58-64. <https://doi.org/10.1016/j.brainresprot.2005.10.002>.
1124 [82] F.G. Martinez, E.E. Hermel, L.L. Xavier, G.G. Viola, J. Riboldi, A.A. Rasia-Filho, M. Achaval,
1125 Gonadal hormone regulation of glial fibrillary acidic protein immunoreactivity in the medial amygdala
1126 subnuclei across the estrous cycle and in castrated and treated female rats, *Brain Res*. 1108 (2006)
1127 117-126. <https://doi.org/10.1016/j.brainres.2006.06.014>.
1128 [83] L. Saur, P.P. Baptista, P.N. de Senna, M.F. Paim, P. do Nascimento, J. Ilha, P.B. Bagatini, M.
1129 Achaval, L.L. Xavier, Physical exercise increases gfap expression and induces morphological
1130 changes in hippocampal astrocytes, *Brain Struct Funct*. 219 (2014) 293-302.
1131 <https://doi.org/10.1007/s00429-012-0500-8>.

1132

1133 **Figures**

1134 *Figures are provided as an attached single pdf document.*

1135

1136 **Figure Captions**

1137 **Figure 1: Experimental design scheme and TEM of the different nanomaterials tested. (A)**

1138 Experimental design of the present study. After stereotactic administration of different nanomaterials,
1139 brains were collected at different time points. Molecular and cellular analyses were performed in the
1140 injection site and in nearby regions (anterior and posterior). **(B)** Transmission electron microscopy
1141 characterisation of the nanomaterials (aminated MWNTs, carboxylated MWNTs, GO, cationic and
1142 anionic liposomes) used in this work.

1143

1144 **Figure 2: RT-qPCR analysis results obtained in the brain striatum injection site. (A)** Gene

1145 expression levels of transcripts encoding pro-inflammatory cytokines, chemokines, and anti-
1146 inflammatory cytokines. The analysis was performed at 1 d, 2 d, and 7 d after injection of LPS, 5%
1147 dextrose, cationic or anionic liposomes (1 µg/µl), MWNT-NH₃⁺ or ox-MWNT (0.5 µg/µl), or GO (0.5
1148 µg/µl). **(B)** Heat map presenting the statistical analysis. All statistical differences are shown in
1149 heatmap colours comparing dextrose with all types of material injected. Mean ± SEM, *p<0.05,
1150 **p<0.01, ***p<0.001 ****p<0.0001 vs 5% dextrose.

1151

1152 **Figure 3: Quantitative analysis of glial cell immunohistochemical staining performed in**
1153 **different brain regions;** anterior to the injection site **(A)**, the injection site **(B)** and a posterior site **(C)**

1154 nearby the injection site. Relative proportion of the area (mean per ROI) covered by microglial
1155 (CD11b-immunopositive) cells **(i)**, or astrocytes (GFAP-immunopositive cells) **(ii)** and estimated
1156 number of neurons (NeuN-immunopositive cells) **(iii)** counted in ROI were performed in the site of
1157 injection and in the regions anterior and posterior at 2 d after administration of LPS, 5% dextrose
1158 (ipsilateral and contralateral sides), MWNT-NH₃⁺ or ox-MWNT or GO (0.5 and 1 µg/µl), or cationic and
1159 anionic liposomes (1 µg/µl). Mean ± SEM; p-values are in comparison to 5% dextrose samples.

1160 *p<0.05, **p<0.01, ****p<0.0001 vs 5% dextrose. Representative images of the different
1161 immunostainings are presented in Figures S5, S6, and S7.

1162

1163 **Figure 4: Representative images of cleaved-caspase 3 immunohistochemical staining.** The
1164 immunophenotyping of cleaved-caspase 3 positive elements (undergoing apoptosis) in the injection
1165 site (the striatum) and in the anterior region distant from the injection site and in the posterior region
1166 adjacent to the injection site obtained at 2 d after injection of LPS, 5% dextrose, GO, and cationic
1167 liposomes. Note that apoptotic elements were visible in the injection site of LPS and cationic
1168 liposomes, while apoptotic cells visible in the GO-injected brain were comparable to the vehicle
1169 control (5% dextrose).

1170 **Table of Content**

1171

1172 Various nanomaterials are been explored for the brain delivery of therapeutic or imaging compounds.

1173 After administration in the brain, Portioli et al. demonstrate in a pilot study that functionalised carbon

1174 based nanomaterials may present a better safety profile than highly charged liposomes. Graphene

1175 Oxide nanosheets could even alleviate the inflammation caused by their direct injection in the brain.

1176

1177 *Corinne Portioli, Cyrill Bussy, Mariarosa Mazza, Neus Lozano, Dhifaf A. Jasim, Maurizio Prato,*

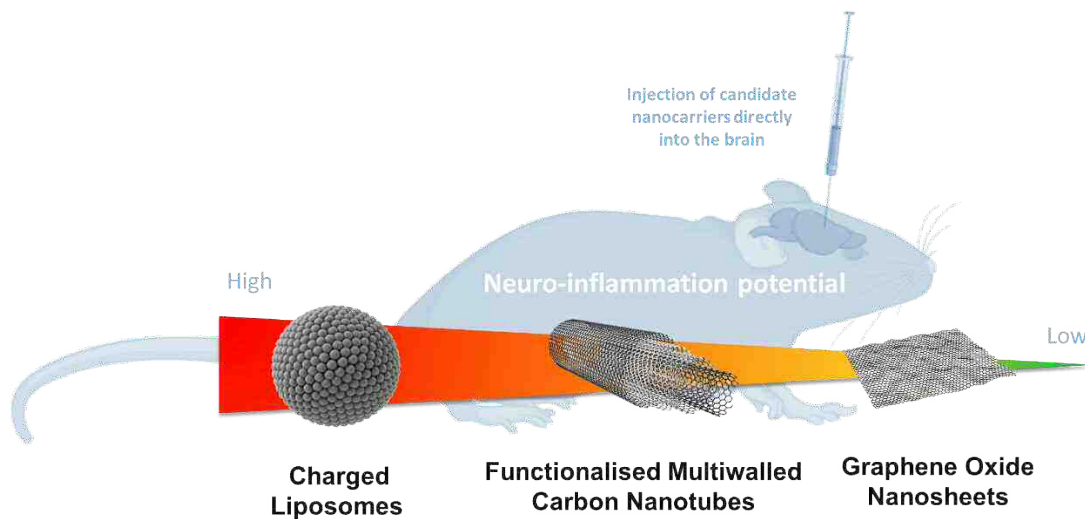
1178 *Alberto Bianco, Marina Bentivoglio and Kostas Kostarelos*

1179

1180 **Injection of Graphene Oxide Nanosheets in the Brain Does not Induce Acute Neurotoxicity**

1181 **and Counteracts the Acute Microglial Activation related to Surgery in a Pilot Study**

1182



1183

1184 **Supplementary Information**

1185 *A supplementary information document with supplementary figures is provided as an attached single*
1186 *pdf document.*

1187

1188 **Supplementary Figure Captions**

1189 **Table S1:** Forward and reverse sequences of the primers used in the present study.

1190

1191 **Table S2:** Primary and secondary antibodies and solutions used for immunohistochemical
1192 procedures.

1193

1194 **Figure S1: Material characteristics.** The different material characteristics (length, amount of
1195 amination and oxidation, zeta-potential, lateral dimensions, polydispersity, and thickness) are
1196 presented for (A) f-MWNTs (MWNT-NH₃⁺ and ox-MWNT), (*) this data was previously published in
1197 Bussy et al. Nanoscale 2016 (ref. 55 in this article), (B) GO sheets, and (C) liposomes (DOTAP:Chol
1198 and DOPG:Chol).

1199

1200 **Figure S2: RT-qPCR analysis of gene expression levels in the brain region posterior to the**
1201 **injection site.** (A) Gene expression levels of transcripts encoding pro-inflammatory cytokines,
1202 chemokines, and anti-inflammatory cytokines. The analysis was performed at 1 d, 2 d, and 7 d after
1203 injection of LPS, 5% dextrose, cationic or anionic liposomes (1 µg/µl), MWNT-NH₃⁺ or ox-MWNT (0.5
1204 µg/µl), or GO (0.5 µg/µl). (B) Heat map presenting the statistical analysis. All statistical differences
1205 are shown in heat map colours comparing dextrose with all types of material injected. Mean ± SEM,
1206 *p<0.05, **p<0.01, ***p<0.001 ****p<0.0001 vs 5% dextrose.

1207

1208 **Figure S3: RT-qPCR analysis of gene expression levels in the brain region anterior to the**
1209 **injection site.** (A) Relative gene expression levels of transcripts encoding pro-inflammatory and anti-
1210 inflammatory cytokines and chemokines obtained at 1 d and 2 d after injection of LPS, 5% dextrose,
1211 cationic or anionic liposomes (1 µg/µl). (B) Heat map presenting the statistical analysis. All statistical
1212 differences are shown in heat map colours comparing dextrose with all types of material injected.
1213 Mean ± SEM, *p<0.05, **p<0.01, ***p<0.001 ****p<0.0001 vs 5% dextrose.

1214

1215 **Figure S4: CD11b immunohistochemical staining of microglia.** (A) Representative images of
1216 microglial cells as visualised by CD11b immunoreactivity in the three analysed brain regions (site of
1217 injection, anterior brain region distant from the site of injection, and posterior brain region adjacent to
1218 the site of injection) at 2 d after the injection of LPS, 5% dextrose, MWNT-NH₃⁺ or ox-MWNT or GO
1219 (0.5 and 1 µg/µl), or cationic or anionic liposomes (1 µg/µl). (B) Densitometric evaluation (in optical
1220 density, or OD units) of the CD11b immunosignal intensity is shown in the injection site at 2 d after

1221 the administration of LPS, 5% dextrose, GO (0.5 and 1 $\mu\text{g}/\mu\text{l}$), or cationic or anionic liposomes (1
1222 $\mu\text{g}/\mu\text{l}$). Mean \pm SEM; the p-value is for the comparison with 5% dextrose samples: * $p < 0.05$, ** $p < 0.01$.

1223

1224 **Figure S5: GFAP immunohistochemical staining of astrocytes.** (A) Representative images of
1225 astrocytes as visualised by GFAP immunoreactivity in the three analysed brain regions (site of
1226 injection, anterior brain region to site of injection, and posterior brain region to site of injection) at 2 d
1227 after the injection of LPS, 5% dextrose, MWNT-NH₃⁺ or ox-MWNT or GO (0.5 and 1 $\mu\text{g}/\mu\text{l}$), or cationic
1228 or anionic liposomes (1 $\mu\text{g}/\mu\text{l}$). (B) Estimated number of astrocytes (per ROI) counted stereologically
1229 at the site of injection and in the regions anterior and posterior is shown at 2 d after injection of LPS,
1230 5% dextrose, or cationic liposomes. Mean \pm SEM; the p value is for the comparison with 5%
1231 dextrose samples: *** $p < 0.001$.

1232

1233 **Figure S6: NeuN immunohistochemical staining of neurons.** Representative images of neuronal
1234 cells as visualised by NeuN immunoreactivity in the three analysed brain regions (site of injection,
1235 anterior brain region to site of injection and posterior brain region to site of injection) at 2 d after the
1236 injection of LPS, 5% dextrose, MWNT-NH₃⁺ or ox-MWNT or GO (0.5 and 1 $\mu\text{g}/\mu\text{l}$), or cationic or
1237 anionic liposomes (1 $\mu\text{g}/\mu\text{l}$). Quantitative evaluation of this staining is presented in Figure 3.

1238

1239 **Figure S7: FluoroJade B staining.** Representative images of Fluoro-Jade B staining in the cerebral
1240 cortex and in the striatum regions of the coronal brain sections containing the injection site at 2 d
1241 after administration of LPS, 5% dextrose, GO, or cationic liposomes. Degenerating neurons, labelled
1242 by green Fluoro-Jade B fluorescent staining, were visible mainly in the LPS- (cortex around the
1243 needle track and striatum) and cationic liposome (striatum)-treated tissues.

1244

1245

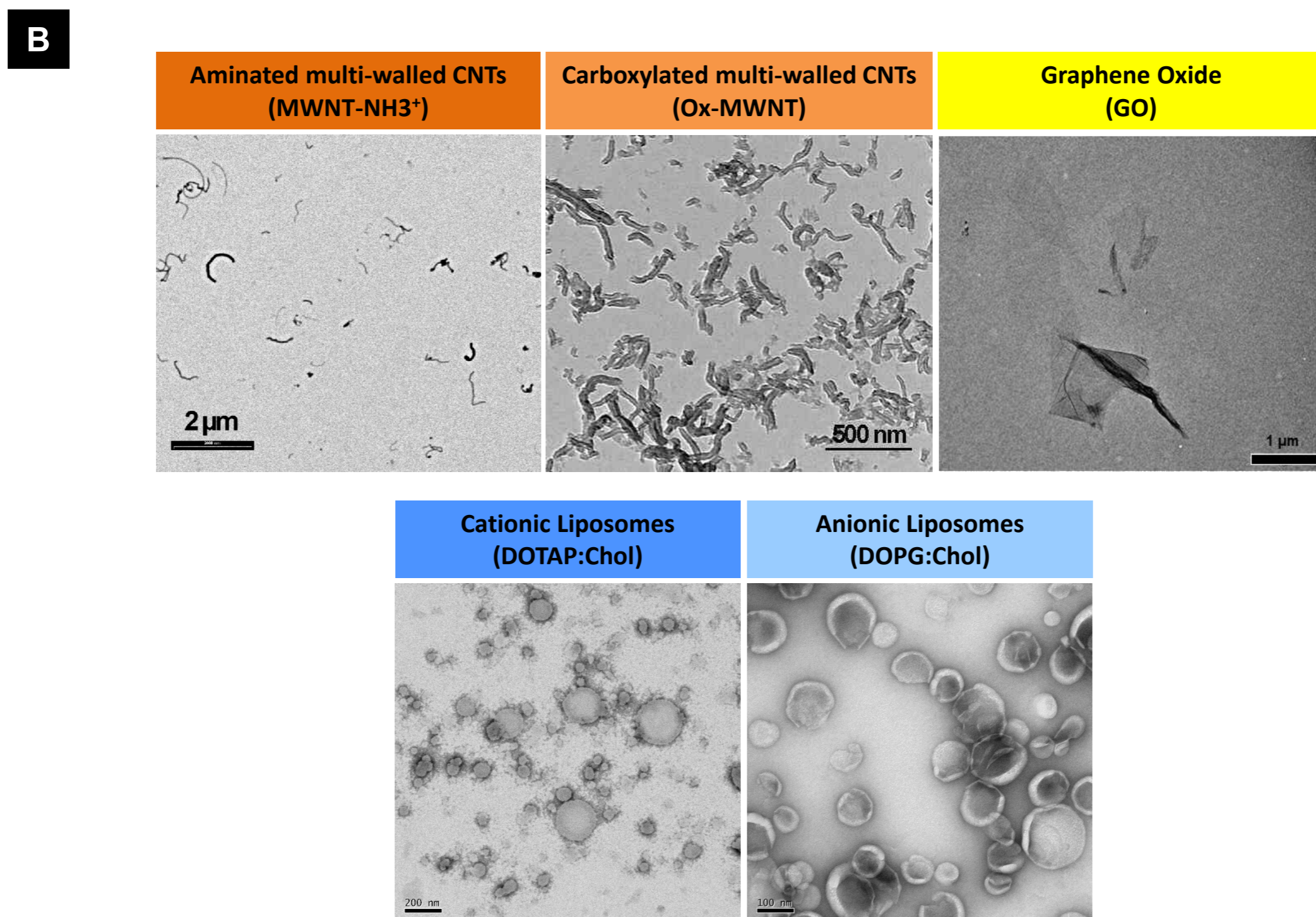
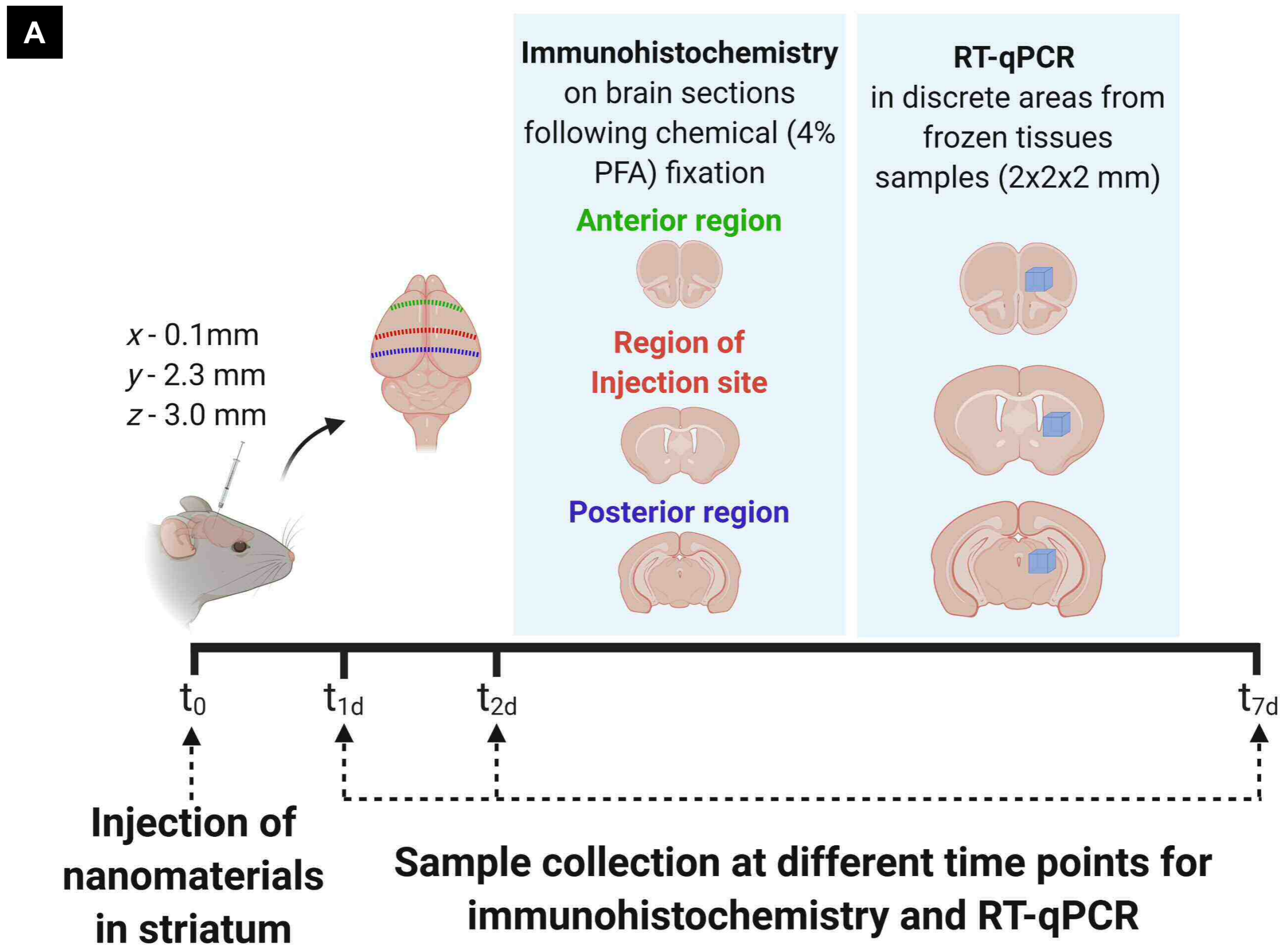
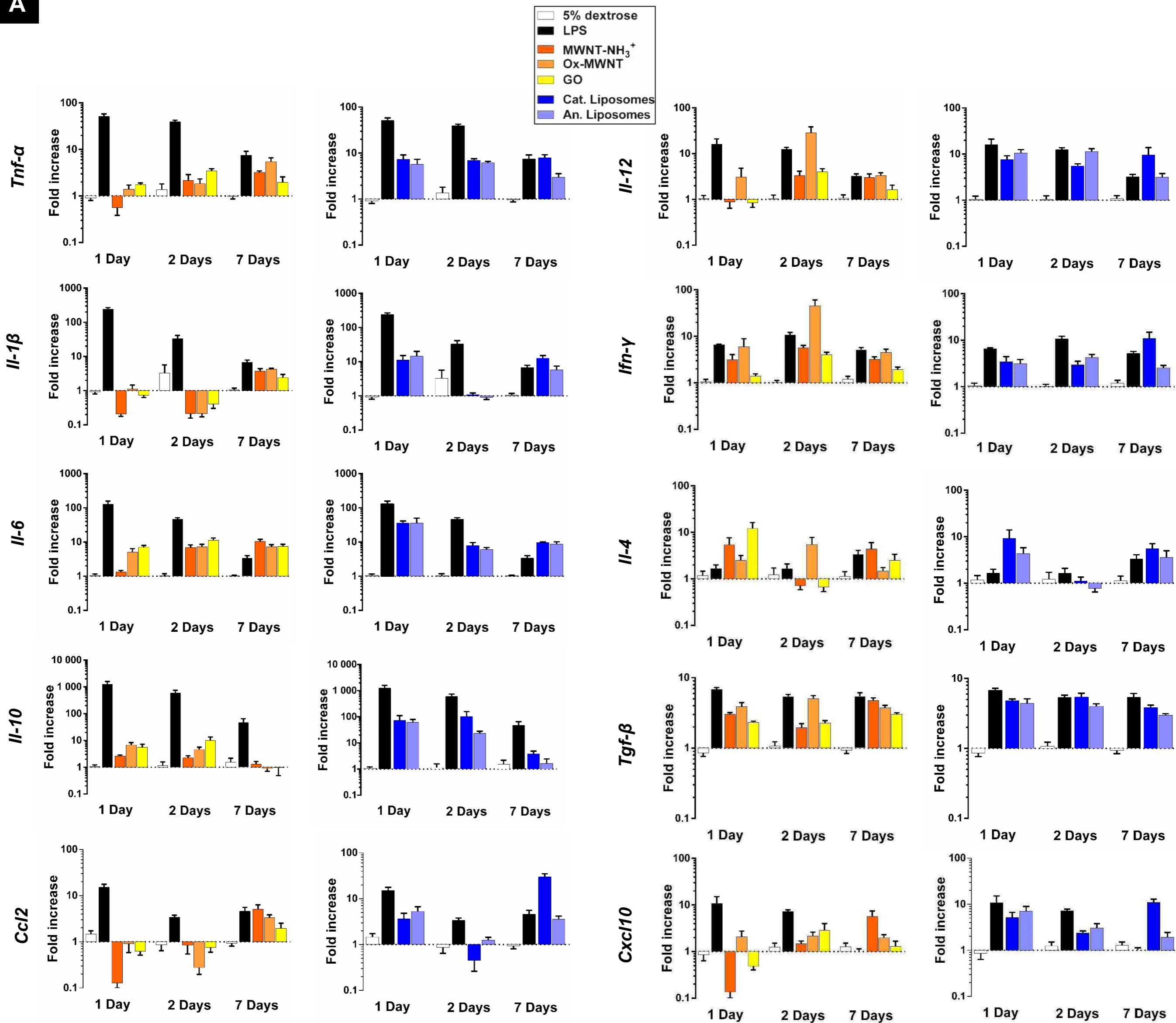
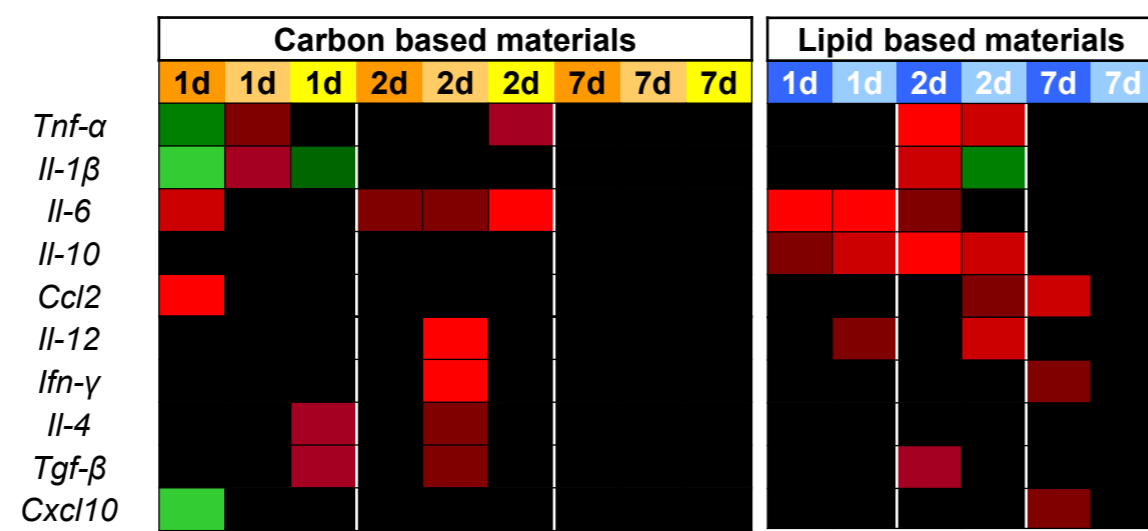


Figure 1

A



B



Upregulated	Downregulated	Statistical difference from 5% dextrose
Red	Green	****; p < 0.0001
Red	Green	***; p < 0.001
Red	Green	**; p < 0.01
Red	Green	*; p < 0.05
Black	Black	ns

Figure 2

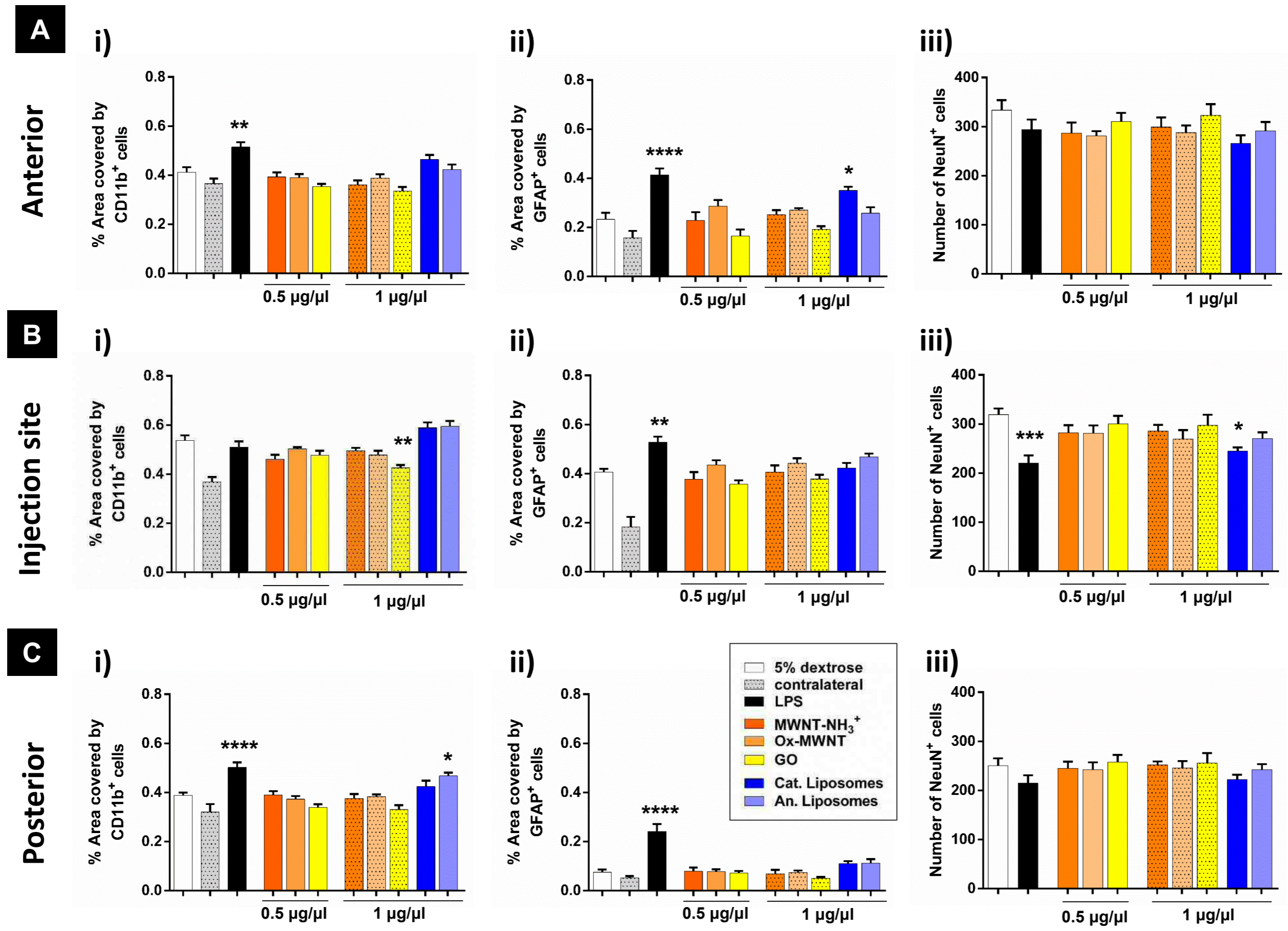


Figure 3

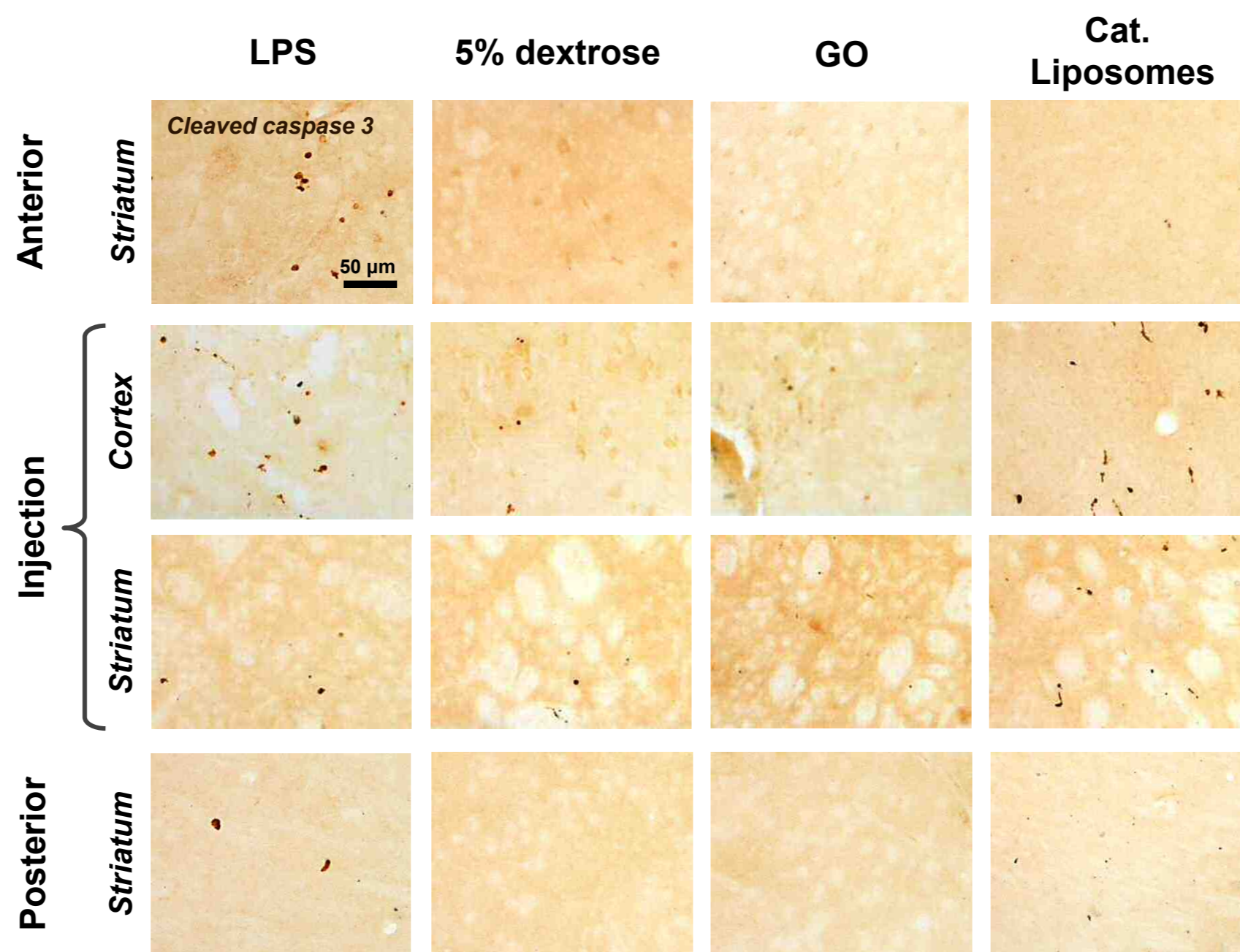


Figure 4

Supplementary Information (Tables and Figures)

Injection of Graphene Oxide Nanosheets in the Brain Does not Induce Acute Neurotoxicity and Counteracts the Acute Microglial Activation related to Surgery in a Pilot Study

Corinne Portioli^{1, 2, §}, Cyrill Bussy^{1, 3, 4 *}, Mariarosa Mazza¹, Neus Lozano^{1, 3}, Dhifaf A. Jasim^{1, 3}, Maurizio Prato^{5, 6}, Alberto Bianco⁷, Marina Bentivoglio² and Kostas Kostarelos^{1, 3, 8, *, &}

¹ *Nanomedicine Lab, School of Health Sciences, Faculty of Biology, Medicine & Health, The University of Manchester, Manchester Academic Health Science Centre, Manchester, UK*

² *Department of Neurosciences, Biomedicine and Movement Sciences, University of Verona, Verona, Italy*

³ *National Graphene Institute, The University of Manchester, Manchester, UK*

⁴ *Lydia Becker Institute of Immunology and Inflammation, Faculty of Biology, Medicine and Health, The University of Manchester, Manchester Academic Health Science Centre, Manchester, UK*

⁵ *Department of Chemical and Pharmaceutical Sciences, University of Trieste, 34127 Trieste, Italy*

⁶ *Carbon Nanobiotechnology Laboratory, CIC BiomaGUNE, 20009 San Sebastian, Spain.*

⁷ *University of Strasbourg, CNRS, Immunology, Immunopathology and Therapeutic Chemistry, UPR 3572, Strasbourg, France*

⁸ *Catalan Institute of Nanoscience and Nanotechnology (ICN2), and The Barcelona Institute of Science and Technology (BIST), Campus UAB, Bellaterra, Barcelona, Spain*

Table S1: Forward and reverse sequences of the primers used in the present study.

Gene	Forward sequence (5'-3')	Reverse sequence (5'-3')
m β -actin	GACCTCTATGCCAACACAGT	AGTACTTGCCTCAGGAGGA
mTNF α	CAGACCCTCACACTCAGATCATCT	CCTCCACTTGGTGGTTTGCTA
mIL-1 β	GGACAGAATATCAACCAACAAGTGATA	GTGTGCCGTCTTTCATTACACAG
mIL-6	ATGGATGCTACCAAAGTGA	CCTCTTGGTTGAAGATATGA
mIL-12	AGAGGTGGACTGGACTCCCG	AGTCTCGCCTCCTTTGTGGC
mINF γ	TCAAGTGGCATAGATGTGGAAGAA	TGGCTCTGCAGGATTTTCATG
mCXCL10	GACGGTCCGCTGCAACTG	GCTCCCTATGGCCCTCATT
mCCL2	CATGCTTCTGGGCCTGCTGTTT	CCTGCTGCTGGTATCCTCTTGTAG
mIL-10	GGTTGCCAAGCCTTATCGGA	ACCTGCTCCACTGCCTTGCT
mTGF β	GACCAGCCGCCGCCGAGG	AGGGCTGTCTGGAGTCTC
mIL-4	GAGACTCTTTCGGCTTTTC	TGATGCTCTTTAGGCTTTCCA

Table S2: Primary and secondary antibodies and solutions used for immunohistochemical procedures.

Marker	Pre-incubation	Primary antibody	Dilution	Supplier	Secondary antibody	Dilution
Neurons	normal horse serum 5%	mouse anti-NeuN	1:500	Millipore, Massachusetts, US	biotinylated horse anti-mouse	1:200
Astrocytes	normal goat serum 5%	rabbit polyclonal anti-GFAP	1:500	Dako, Carpinteria, US	biotinylated goat anti-rabbit	1:200
Microglial cells	normal goat serum 5%	rat anti-CD11b	1:500	AbD Serotec, Oxford, UK	biotinylated goat anti-rat	1:200
Apoptotic cells	normal horse serum 5%	rabbit anti-cleaved caspase 3 (Asp175)	1:600	Cell Signaling, Danvers, US	biotinylated horse anti-rabbit	1:200

A	Measurement	Aminated multi-walled CNTs (MWNT-NH ₃ ⁺) cycloaddition	Carboxylated multi-walled CNTs (Ox-MWNT) acidic treatment
	Length (TEM)	500 – 2000 nm	200 – 300 nm
	Diameter (TEM)	20 - 30 nm	20 - 30 nm
	Amount of amination (Kaiser test)	58 μmol/g	-
	Amount of carboxyl groups (TGA)	-	1,7 μmol/g (*)

B	Measurement	Graphene Oxide Sheets (GO)
	Zeta potential	-50.0 ± 0.4 mV
	Lateral dimensions (TEM)	10 – 1800 nm
	Thickness (AFM)	0.9 - 4.8 nm

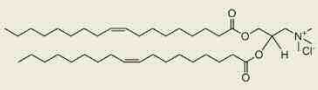
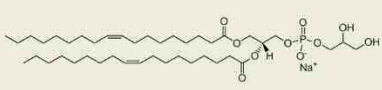
C	Measurement	Cationic Liposomes, DOTAP:Chol (2:1)	Anionic Liposomes, DOPG:Chol (2:1)
			
	Zeta potential	- 54.1 ± 0.5 mV	+ 60.5 ± 2.6 mV
	Hydrodynamic diameter (DLS)	118.1 ± 3.0 nm	125.6 ± 2.6 nm
	Polydispersity	0.329 ± 0.022	0.250 ± 0.007

Figure S1: Material characteristics. The different material characteristics (length, amount of amination and oxidation, zeta-potential, lateral dimensions, polydispersity, and thickness) are presented for **(A)** *f*-MWNTs (MWNT-NH₃⁺ and ox-MWNT), (*) this data was previously published in Bussy et al. Nanoscale 2016 (ref. 55 in this article), **(B)** GO sheets, and **(C)** liposomes (DOTAP:Chol and DOPG:Chol).

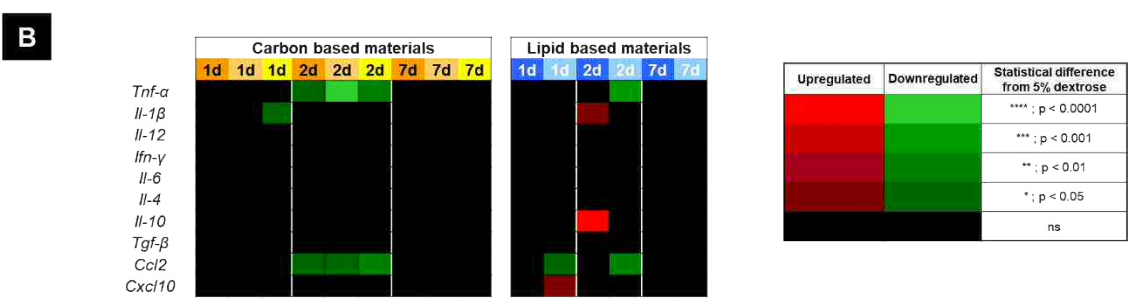
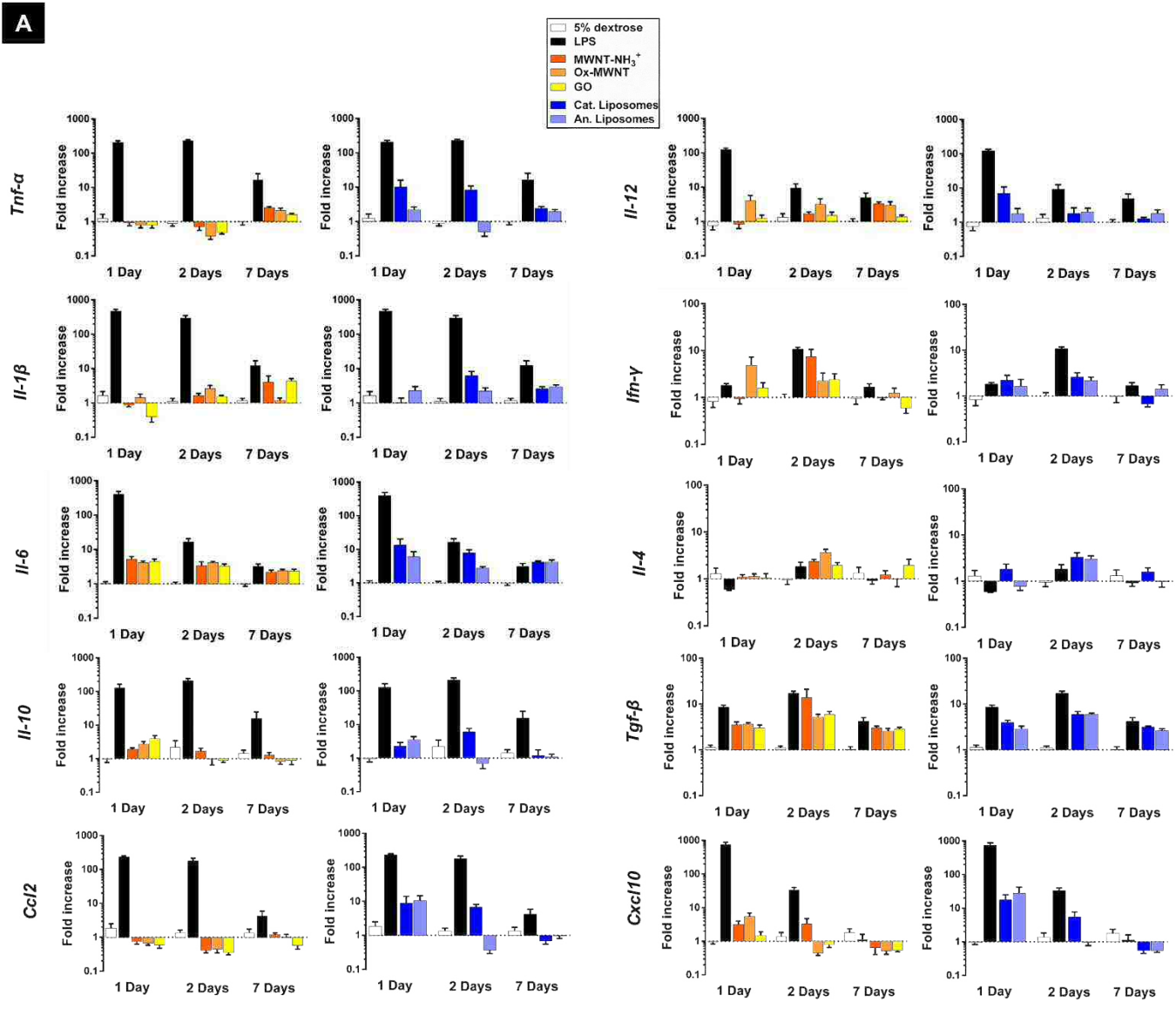


Figure S2: RT-qPCR analysis of gene expression levels in the brain region posterior to the injection site. (A) Gene expression levels of transcripts encoding pro-inflammatory cytokines, chemokines, and anti-inflammatory cytokines. The analysis was performed at 1 d, 2 d, and 7 d after injection of LPS, 5% dextrose, cationic or anionic liposomes (1 μg/μl), MWNT-NH₃⁺ or ox-MWNT (0.5 μg/μl), or GO (0.5 μg/μl). **(B)** Heat map presenting the statistical analysis. All statistical differences are shown in heat map colours comparing dextrose with all types of material injected. Mean ± SEM, *p<0.05, **p<0.01, ***p<0.001 ****p<0.0001 vs 5% dextrose.

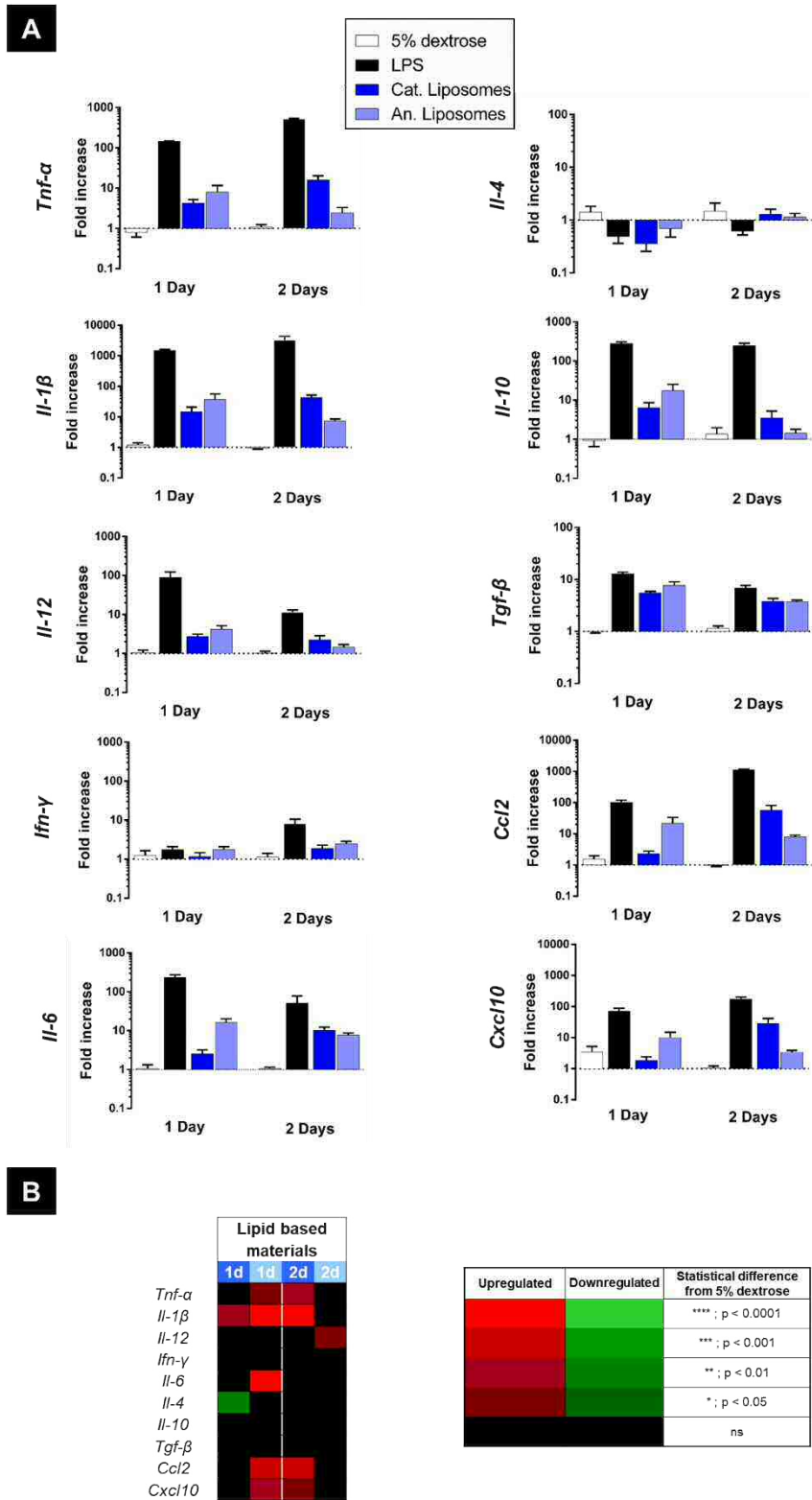


Figure S3: RT-qPCR analysis of gene expression levels in the brain region anterior to the injection site. (A) Relative gene expression levels of transcripts encoding pro-inflammatory and anti-inflammatory cytokines and chemokines obtained at 1 d and 2 d after injection of LPS, 5% dextrose, cationic or anionic liposomes (1 $\mu\text{g}/\mu\text{l}$). **(B)** Heat map presenting the statistical analysis. All statistical differences are shown in heat map colours comparing dextrose with all types of material injected. Mean \pm SEM, * $p < 0.05$, ** $p < 0.01$, *** $p < 0.001$ **** $p < 0.0001$ vs 5% dextrose.

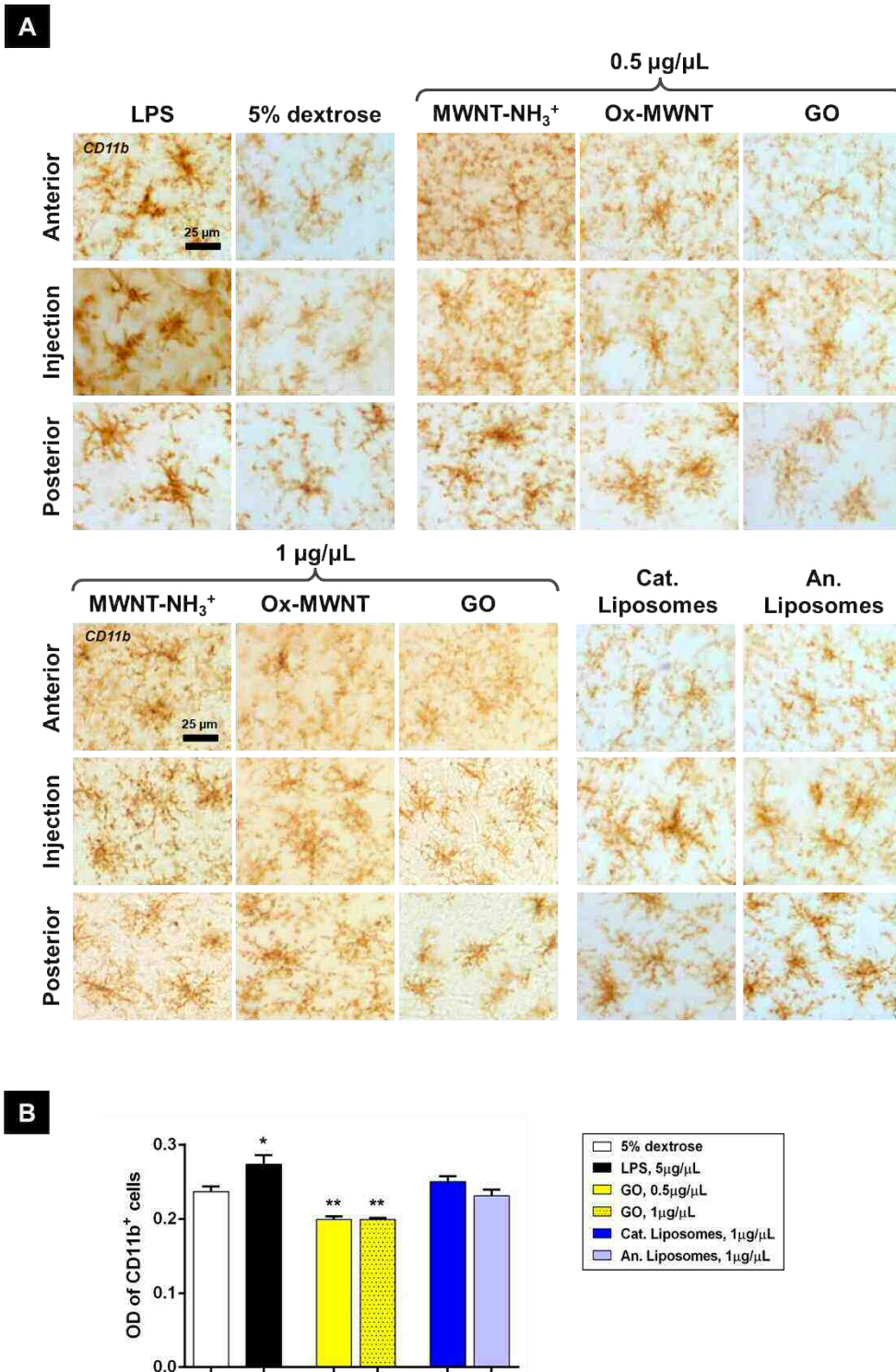


Figure S4: CD11b immunohistochemical staining of microglia. (A) Representative images of microglial cells as visualised by CD11b immunoreactivity in the three analysed brain regions (site of injection, anterior brain region distant from the site of injection, and posterior brain region adjacent to the site of injection) at 2 d after the injection of LPS, 5% dextrose, MWNT-NH₃⁺ or ox-MWNT or GO (0.5 and 1 µg/µl), or cationic or anionic liposomes (1 µg/µl). (B) Densitometric evaluation (in optical density, or OD units) of the CD11b immunosignal intensity is shown in the injection site at 2 d after the administration of LPS, 5% dextrose, GO (0.5 and 1 µg/µl), or cationic or anionic liposomes (1 µg/µl). Mean ± SEM; the p-value is for the comparison with 5% dextrose samples: *p<0.05, **p<0.01.

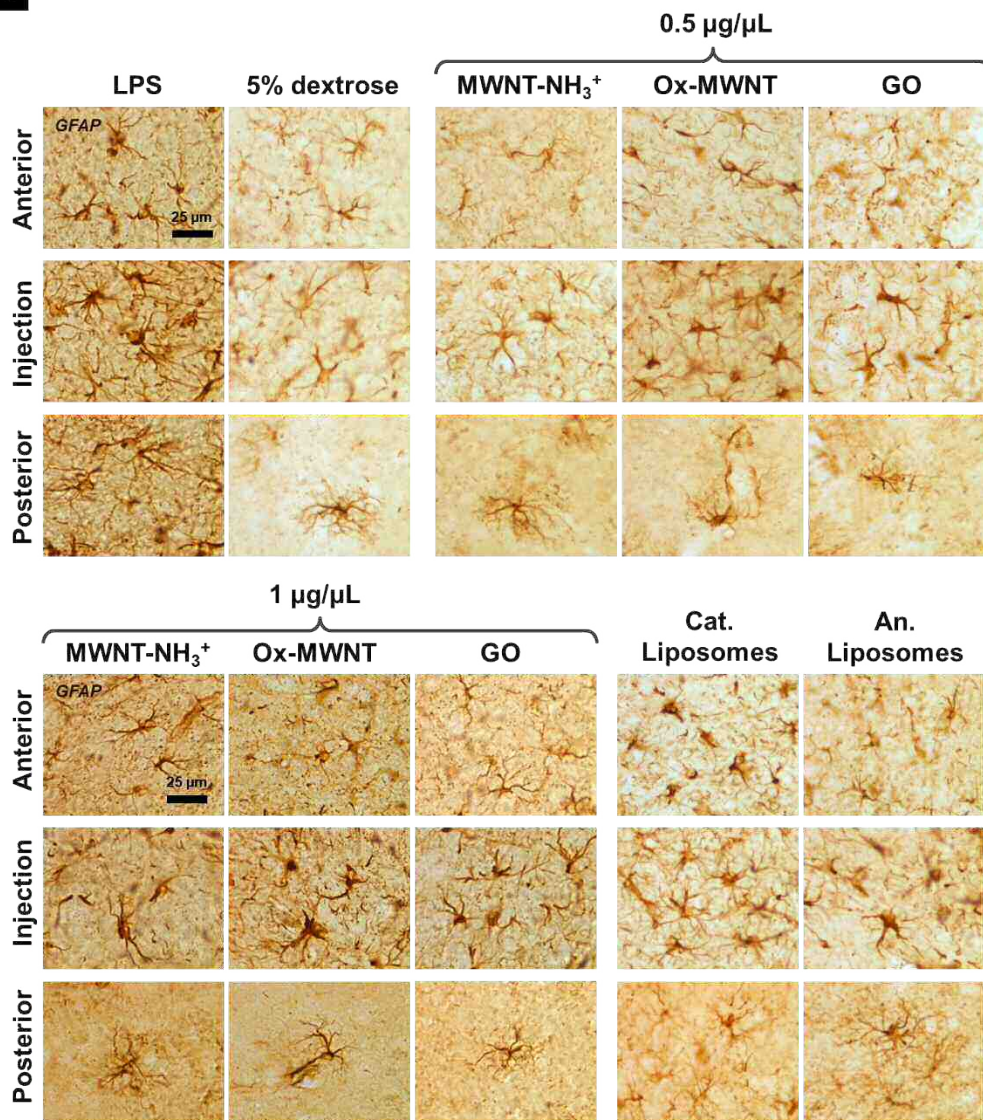
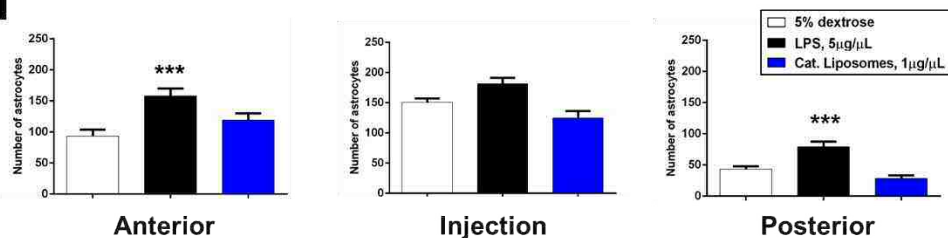
A**B**

Figure S5: GFAP immunohistochemical staining of astrocytes. (A) Representative images of astrocytes as visualised by GFAP immunoreactivity in the three analysed brain regions (site of injection, anterior brain region to site of injection, and posterior brain region to site of injection) at 2 d after the injection of LPS, 5% dextrose, MWNT-NH₃⁺ or ox-MWNT or GO (0.5 and 1 µg/µl), or cationic or anionic liposomes (1 µg/µl). (B) Estimated number of astrocytes (per ROI) counted stereologically at the site of injection and in the regions anterior and posterior is shown at 2 d after injection of LPS, 5% dextrose, or cationic liposomes. Mean ± SEM; the p value is for to the comparison with 5% dextrose samples: ***p<0.001.

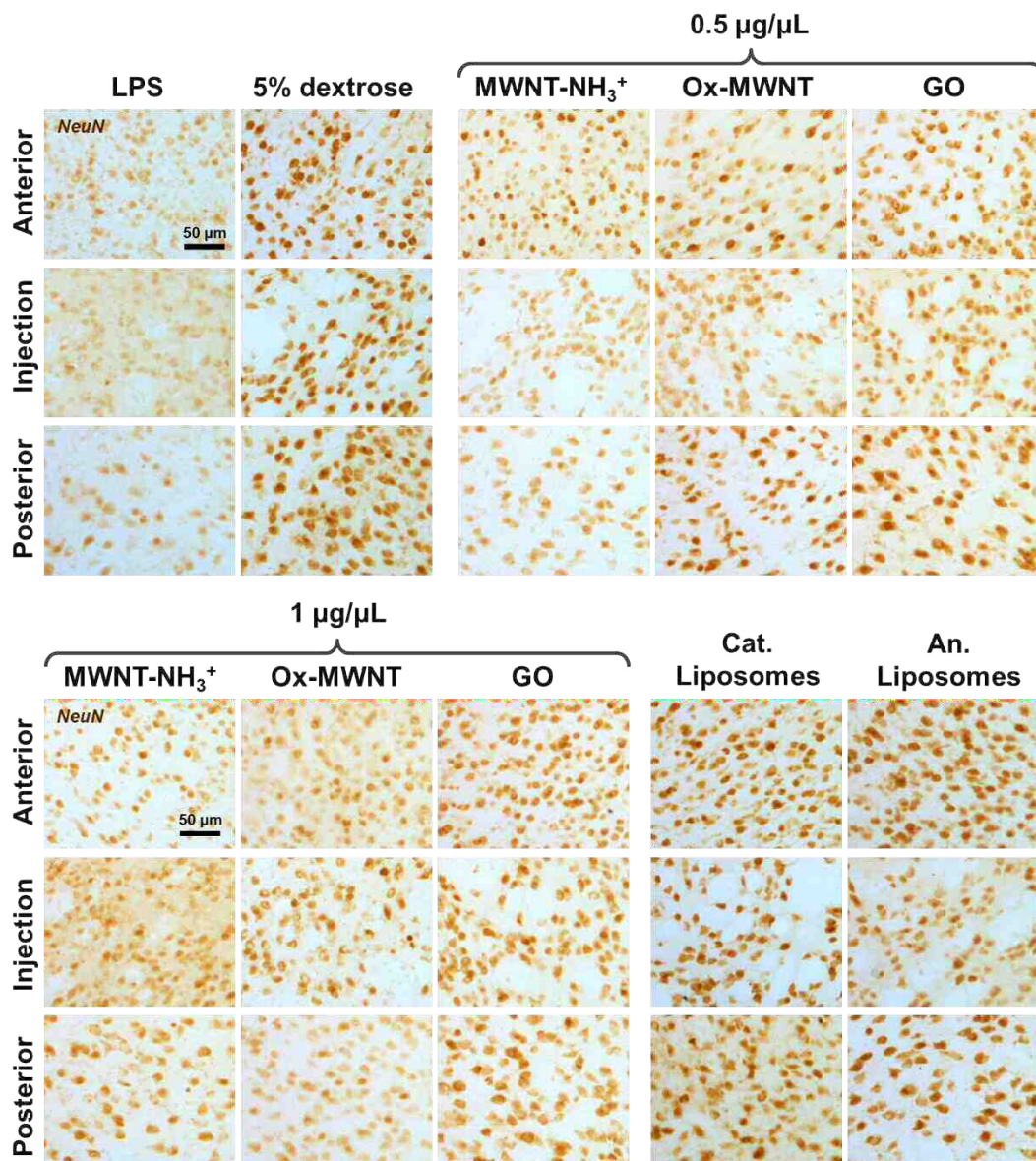


Figure S6: NeuN immunohistochemical staining of neurons. Representative images of neuronal cells as visualised by NeuN immunoreactivity in the three analysed brain regions (site of injection, anterior brain region to site of injection and posterior brain region to site of injection) at 2 d after the injection of LPS, 5% dextrose, MWNT-NH₃⁺ or ox-MWNT or GO (0.5 and 1 µg/µl), or cationic or anionic liposomes (1 µg/µl). Quantitative evaluation of this staining is presented in Figure 3.

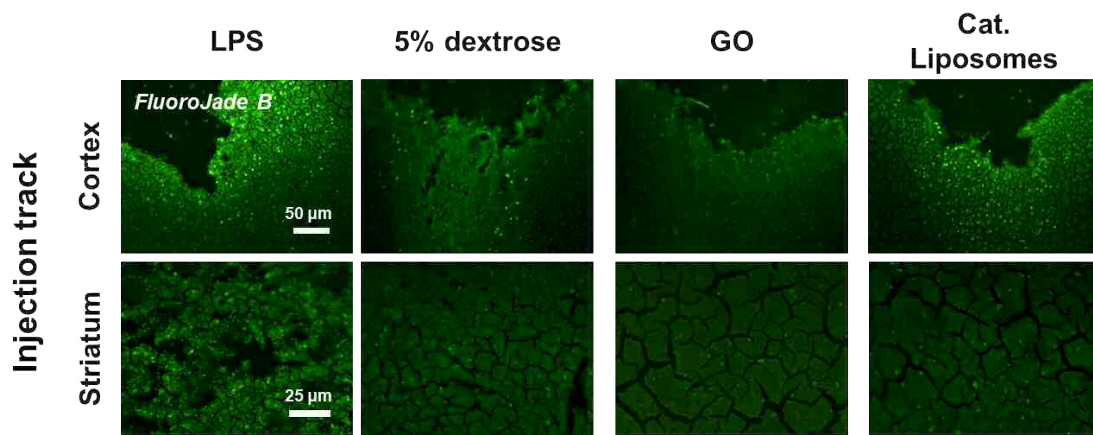


Figure S7: FluoroJade B staining. Representative images of Fluoro-Jade B staining in the cerebral cortex and in the striatum regions of the coronal brain sections containing the injection site at 2 d after administration of LPS, 5% dextrose, GO, or cationic liposomes. Degenerating neurons, labelled by green Fluoro-Jade B fluorescent staining, were visible mainly in the LPS- (cortex around the needle track and striatum) and cationic liposome (striatum)-treated tissues.